iScience

CellPress
OPEN ACCESS

Article

Monitoring GPCR conformation with GFP-inspired dyes

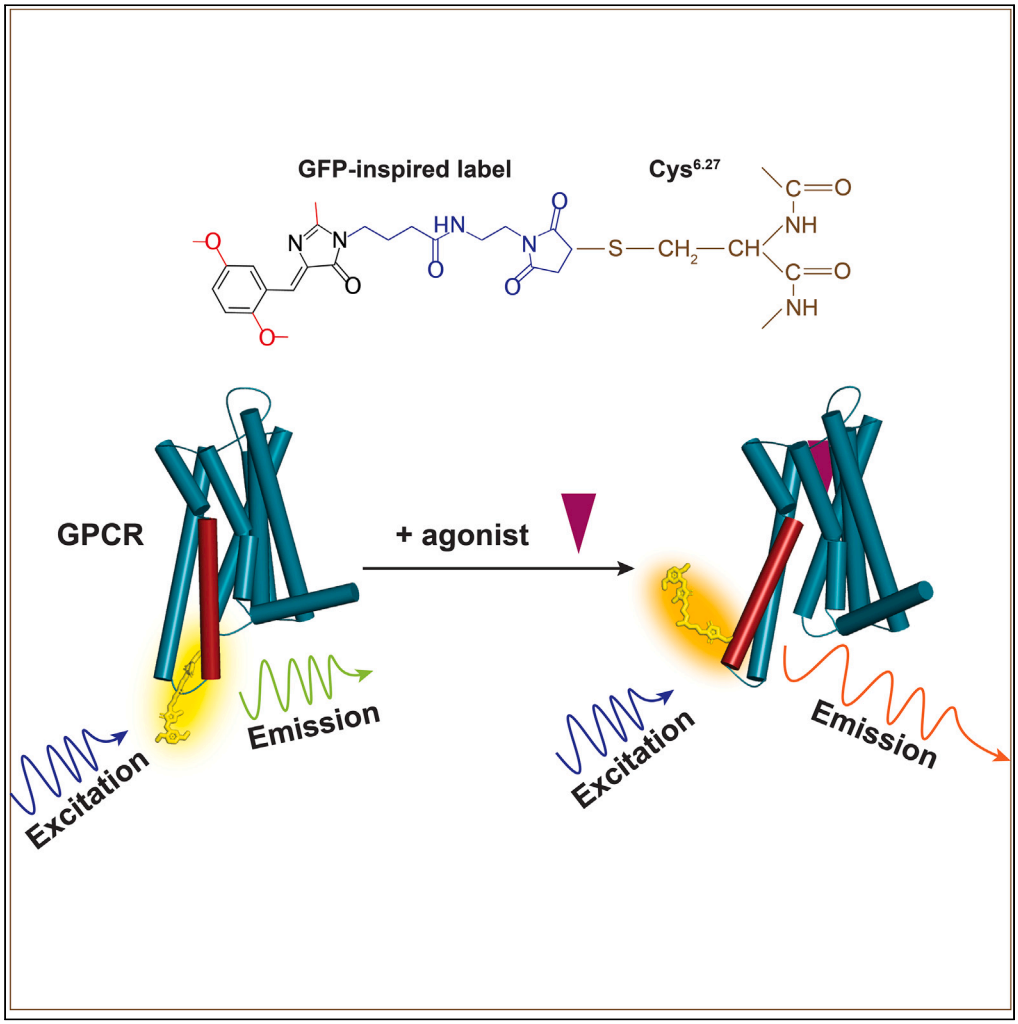

Anatoliy Belousov, Ivan Maslov, Philipp Orekhov, ..., Mikhail Baranov, Alexey Mishin, Valentin Borshchevskiy

borshchevskiy@gmail.com

Highlights

GFP-inspired dyes can detect structural changes in GPCRs

DyeC responds to changes induced by allosteric modulator and orthosteric agonists

Conformational changes can be tracked ratiometrically and by fluorescence intensity

Belousov et al., iScience 27, 110466
August 16, 2024
https://doi.org/10.1016/j.isci.2024.110466

iScience

CellPress
OPEN ACCESS

Article

Monitoring GPCR conformation with GFP-inspired dyes

Anatoliy Belousov,[1,16] Ivan Maslov,[1,2,3,16] Philipp Orekhov,[4,5,16] Polina Khorn,[1] Pavel Kuzmichev,[1] Nadezhda Baleeva,[6,7] Vladislav Motov,[1,6] Andrey Bogorodskiy,[1] Svetlana Krasnova,[6,8] Konstantin Mineev,[1,6,15] Dmitry Zinchenko,[9] Evgeni Zernii,[10] Valentin Ivanovich,[1] Sergei Permyakov,[11] Johan Hofkens,[3,12] Jelle Hendrix,[2,3] Vadim Cherezov,[13] Thomas Gensch,[3] Alexander Mishin,[6] Mikhail Baranov,[6,7] Alexey Mishin,[1] and Valentin Borshchevskiy[1,14,17,*]

SUMMARY

Solvatochromic compounds have emerged as valuable environment-sensitive probes for biological research. Here we used thiol-reactive solvatochromic analogs of the green fluorescent protein (GFP) chromophore to track conformational changes in two proteins, recoverin and the A_{2A} adenosine receptor (A_{2A}AR). Two dyes showed Ca^{2+}-induced fluorescence changes when attached to recoverin. Our best-performing dye, DyeC, exhibited agonist-induced changes in both intensity and shape of its fluorescence spectrum when attached to A_{2A}AR; none of these effects were observed with other common environment-sensitive dyes. Molecular dynamics simulations showed that activation of the A_{2A}AR led to a more confined and hydrophilic environment for DyeC. Additionally, an allosteric modulator of A_{2A}AR induced distinct fluorescence changes in the DyeC spectrum, indicating a unique receptor conformation. Our study demonstrated that GFP-inspired dyes are effective for detecting structural changes in G protein-coupled receptors (GPCRs), offering advantages such as intensity-based and ratiometric tracking, redshifted fluorescence spectra, and sensitivity to allosteric modulation.

INTRODUCTION

From *in vivo* imaging to single-molecule tracking, the green fluorescent protein (GFP) has become an indispensable tool for many biological studies.[1] The GFP chromophore, 4-hydroxybenzylidene-dimethylimidazolinone (HBDI, Figure 1), is spontaneously formed through the specific cyclization of three amino acid residues located in the center of the GFP β-barrel. Structurally modified synthetic analogs of the GFP chromophore represent a diverse class of benzylidene imidazolones (BDIs) that found many applications as versatile labels due to their exceptional fluorescent properties, small size, and easy synthesis.[2] Similar to GFP, where the high fluorescence yield of HBDI is supported by the protein microenvironment, the transition of some BDI derivatives from water to less polar solvents results in a substantial increase in their fluorescence quantum yield (FQY). Such compounds have been extensively tested as fluorogenic environmentally sensitive dyes.[3–6] In live-cell imaging, BDI derivatives have been used to stain bacteria[7] or various organelles in eukaryotic cells.[8–12] Fluorogenic BDI derivatives have found extensive application in RNA aptamer-based fluorescent sensors, facilitating the monitoring of transcription and RNA trafficking in cells[13] or cell-free systems,[14] as well as the detection of proteins or intracellular metabolites.[15] BDI-based sensors have also been utilized to track protein misfolding and aggregation.[16]

Ligand-induced conformational changes in proteins are commonly investigated using environmentally sensitive labels.[17–23] Typically, in this approach, thiol-reactive derivatives of the dyes are attached to cysteine residues (either intentionally introduced or naturally present)

[1]Moscow Institute of Physics and Technology, Dolgoprudny 141701, Russia
[2]Dynamic Bioimaging Lab, Advanced Optical Microscopy Centre, Biomedical Research Institute, Agoralaan C (BIOMED), Hasselt University, 3590 Diepenbeek, Belgium
[3]Laboratory for Photochemistry and Spectroscopy, Division for Molecular Imaging and Photonics, Department of Chemistry, KU Leuven, 3001 Leuven, Belgium
[4]Faculty of Biology, Shenzhen MSU-BIT University, Shenzhen 518172, China
[5]Sechenov University, Moscow 119146, Russia
[6]Institute of Bioorganic Chemistry, Russian Academy of Sciences, Moscow 117997, Russia
[7]Pirogov Russian National Research Medical University, Moscow 117997, Russia
[8]National Research University Higher School of Economics, Moscow 101000, Russia
[9]Branch of Shemyakin and Ovchinnikov Institute of Bioorganic Chemistry, Russian Academy of Sciences, Pushchino 142290, Russia
[10]Belozersky Institute of Physico-Chemical Biology, Lomonosov Moscow State University, Moscow 119992, Russia
[11]Institute for Biological Instrumentation, Russian Academy of Sciences, Pushchino 142292, Russia
[12]Max Plank Institute for Polymer Research, Mainz, Germany
[13]Department of Chemistry, University of Southern California, Los Angeles, CA 90089, USA
[14]Joint Institute for Nuclear Research, Dubna 141980, Russian Federation
[15]Present address: Goethe-University Frankfurt, Frankfurt, Germany
[16]These authors contributed equally
[17]Lead contact
*Correspondence: borshchevskiy@gmail.com
https://doi.org/10.1016/j.isci.2024.110466

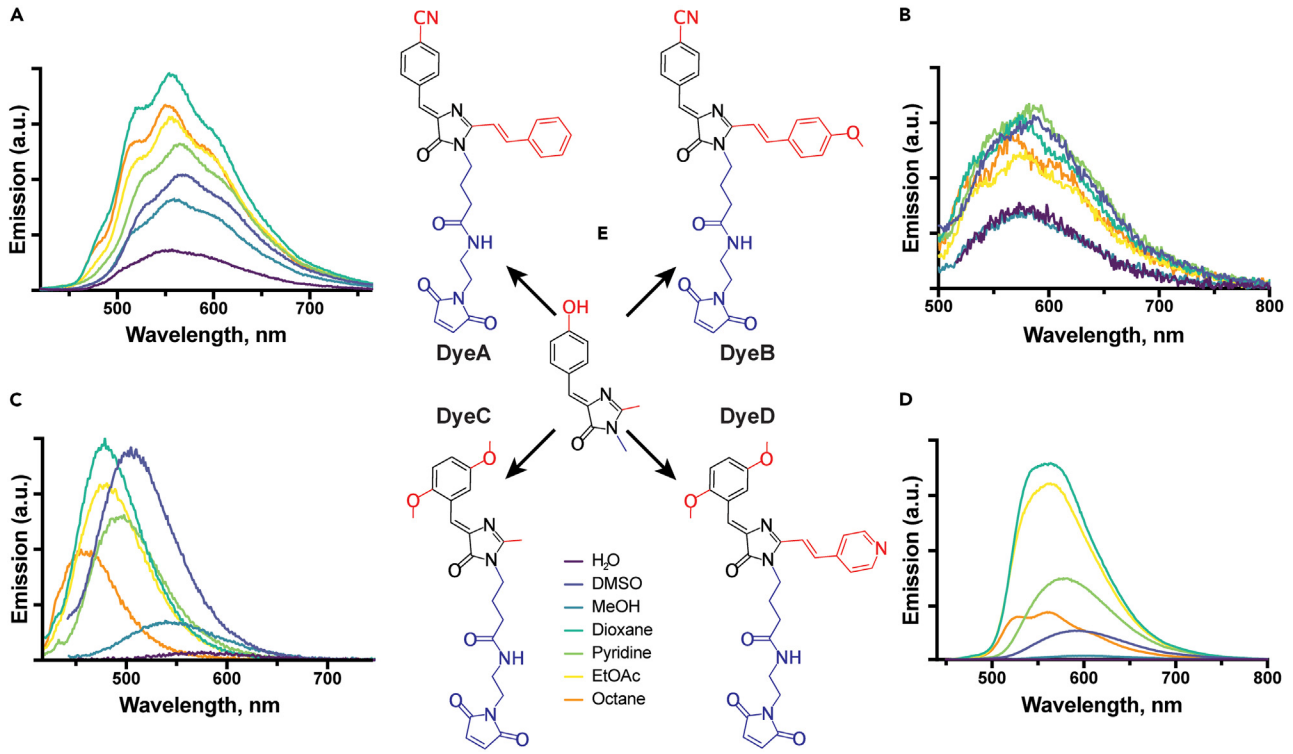

Figure 1. Dye structures and their emission spectra in various solvents

(A–D) Changes of the emission fluorescence spectra for free DyeA (A), DyeB (B), DyeC (C), and DyeD (D) in solvents with different polarity and viscosity. The excitation wavelengths were 410 nm (DyeA), 430 nm (DyeB), 380 nm (DyeC), and 420 nm (DyeD). Complete results and additional information for the tested dyes are provided in Table S1.

(E) The HBDI fluorescent core is shown in the center and four dyes as its derivatives; the maleimide groups, responsible for cysteine interaction, are colored in blue; the fluorescent core modifications are colored in red.

located in the vicinity of functionally labile protein elements. In successful constructs, the fluorescence properties of the label serve as indicators of protein activation or inhibition. These studies shed light on the molecular mechanisms of protein activation and, in some cases, facilitated the design of biomolecular sensors for a wide variety of metabolites.[19,24–29] Despite the wide range of applications, GFP-inspired labels have not been previously utilized for this purpose. In this study, we demonstrate that these labels can serve as environmentally sensitive probes to monitor conformational changes in G protein-coupled receptors (GPCRs).

GPCRs constitute the largest class of membrane proteins in humans that regulate critical physiological processes, e.g., vision, taste, neurotransmission, and inflammation. More than one-third of drugs approved by the United States Food and Drug Administration (FDA) have GPCRs as their primary targets.[30] Most of these drugs target the primary extracellular binding site that naturally accommodates endogenous ligands, i.e., the orthosteric ligand-binding pocket. The ligand binding causes structural changes propagating across the receptor toward the intracellular side and enables coupling to its cognate G proteins or other intracellular partners. In the absence of ligands, most GPCRs exhibit a certain level of activity known as basal signaling. Orthosteric ligands can directly control GPCR activity: agonists increase the basal signaling, antagonists occupy the ligand-binding site but do not affect the receptor's activity, and inverse agonists decrease the basal signaling.[31] The affinity and efficacy of orthosteric ligands can be affected by allosteric modulators that bind to spatially distinct sites on GPCRs and modulate their function.[32–35] Notably, some allosteric modulators can affect the receptor's activation on their own.[34–38]

The A_{2A} adenosine receptor (A_{2A}AR), one of the most studied GPCRs, is a promising target for drugs against cancer, chronic pain, sleep disorders, depression, and Parkinson's disease.[39] It regulates cardiovascular system and inflammation throughout the body and modulates the neurotransmission of glutamate and dopamine in the brain.[40,41] A_{2A}AR has often been used as a prototypical receptor for the development of biophysical techniques for studying other GPCRs.[42–46]

Here we assessed four GFP-inspired fluorophores for their potential to serve as environmentally sensitive labels to report on conformational changes in proteins. For this, we attached a maleimide group to them for cysteine labeling and studied their spectral properties in solvents with varying polarity and viscosity. The best of them were then employed to label two proteins: bovine recoverin (Rec) and A_{2A}AR. We used Rec as a convenient model protein to evaluate the performance of environmentally sensitive labels. This choice is justified by the presence of a sole cysteine residue and the considerable conformational changes induced upon activation by Ca^{2+}. Next, using the best-performing dye attached to A_{2A}AR, we investigated effects of various ligands, including antagonists, agonists, and an allosteric modulator, on its

fluorescence and observed reliable and distinctive changes. Furthermore, we compared this new dye with other dyes, previously used for detecting ligand-induced changes in GPCRs and found that none of them surpassed the performance of the new dye. Finally, we conducted molecular dynamic (MD) simulations of $A_{2A}AR$ labeled with the dyes to gain structural insights into the observed changes.

RESULTS

Synthetic thiol-reactive GFP-inspired fluorophores show solvatochromism

To follow conformational changes in proteins using GFP-inspired fluorophores, we selected BDI derivatives that previously showed solvatochromic properties. It has been reported that the FQY of 4-nitrile and 2,5-dimethoxy derivatives of a BDI benzylidene fragment with the absorption maxima in the UV range depends on the solvent.[47,48] Since fluorophores with redshifted absorption spectra are preferred in many quantitative fluorescence-based measurements due to their lower phototoxicity, background autofluorescence, and scattering, we used their BDI derivatives, which have shown a redshifted absorption together with a remarkable solvatochromism of their emission maxima and high FQY.[3] Therefore, we selected two 4-nitrile (Figure 1, DyeA and DyeB) and two 2,5-dimethoxy (Figure 1, DyeC and DyeD) benzylidene derivatives of redshifted BDI compounds and complemented them with a maleimide group to enable covalent binding to cysteine residues.

To assess the solvatochromism of the maleimide-conjugated compounds, we investigated their fluorescence properties in solvents with different polarities ranging from water to pentadecane (Figure 1, Table S1). Similarly to the original compounds, all four dyes showed notable changes in their fluorescence emission spectra depending on the solvent. We observed that FQYs of the 4-nitrile benzylidene compounds (DyeA and DyeB) strongly depend on the solvent polarity, while the wavelengths of their emission maxima vary by <10 nm in different solvents. At the same time, the 2,5-dimethoxy benzylidene compounds (DyeC and DyeD) showed solvent-dependent changes in both FQY and the wavelength of their emission maxima.

Fluorescence of GFP-inspired dyes highlights Ca^{2+}-dependent conformational changes in Rec

To select dyes suitable for tracking ligand-induced structural changes in proteins, we used a water-soluble protein Rec. Rec is a 23 kDa member of the neuronal calcium sensor family,[49] which participates in regulation of phototransduction and light adaptation of retinal photoreceptors.[50] Rec has two calcium binding sites, and the interaction with calcium ions results in substantial changes in its structure.[51] Rec contains a single cysteine residue, which is conveniently located in the protein loop subjected to structural changes upon activation.[52] The emission spectrum of the Alexa 647 label bound to this cysteine was shown to undergo substantial changes depending on the calcium concentration.[19] All these results and considerations make Rec a perfect test object to validate whether our modified BDI fluorescent labels can report structural changes in a protein.

We labeled Rec with each of the four synthesized maleimide dyes. The absorption spectra of labeled Rec (Figure S1A) showed high labeling efficiencies for DyeA, DyeB, and DyeC (~90%–100%), while DyeD had a low labeling efficiency (<5%) and, therefore, was excluded from further experiments. The low labeling efficiency is probably related to the low water solubility of DyeD that was originally observed for its parent compound (5d compound in Smirnov et al.[3]).

We measured fluorescence emission spectra of the labeled Rec in Ca^{2+}-bound and Ca^{2+}-free states (Figure 2). Rec-DyeB and Rec-DyeC displayed pronounced Ca^{2+}-induced changes in their fluorescence spectra. Similarly to previously characterized solvatochromic properties of DyeB, Rec-DyeB showed a higher emission intensity in the presence of calcium; however, its emission maximum was also redshifted by >50 nm, while the emission wavelength of free DyeB did not exhibit a solvatochromic behavior. On the other hand, Rec-DyeC showed a 50 nm redshift of the emission maximum as expected from the solvatochromic behavior of the free dye, but without any changes in the fluorescence intensity. We further tested the labeling specificity for our best-performing dye, DyeC, and observed that the efficiency of non-specific labeling of the cysteine-free Rec mutant Rec_{C39D} was negligible (<5%, Figure S1A), suggesting that C39 was the only labeled amino acid in the wild-type (WT) protein.

Fluorescence of DyeC highlights conformational changes in $A_{2A}AR$ induced by agonists and an allosteric modulator

To track ligand-induced conformational changes in a GPCR, we labeled $A_{2A}AR$ with DyeB and DyeC. For this purpose, we introduce a cysteine residue $L225^{6.27}C$ (superscripts indicate Ballesteros–Weinstein numbering[54]) at the intracellular tip of the transmembrane helix 6 (TM6) to serve as a labeling site. A large-scale movement of the intracellular part of TM6 is one of the hallmarks of activation in class A (rhodopsin-like) GPCRs,[55] including $A_{2A}AR$.[56] Similar label placements at the intracellular tip of TM6 were used in previous fluorescence-based[57,58] and F^{19}-NMR[43,59,60] studies.

The WT $A_{2A}AR$ ($A_{2A}AR_{WT}$) contains 6 native unpaired cysteines buried in the receptor core, which are available for labeling when the receptor is purified in micelles.[61] To attach dyes only to the genetically introduced cysteine residues, we labeled $A_{2A}AR_{L225C}$ in isolated crude membranes, as described previously.[58,61] This approach enables selective cysteine labeling on the intracellular receptor surface without the necessity of removing native cysteines. After labeling, $A_{2A}AR_{L225C}$ was purified and reconstituted in lipid nanodiscs (NDs). The labeling efficiency was estimated as 80% for $A_{2A}AR_{L225C}$-DyeC and <5% for $A_{2A}AR_{L225C}$-DyeB (Figure S1B); therefore, DyeB was excluded from further experiments. Similar to DyeD, DyeB demonstrated low solubility in water, which correlates with its diminished labeling efficiency. Increased hydrophobicity can induce dyes' precipitation or non-specific binding to cell membranes, thereby diminishing the pool of dye molecules available for labeling.

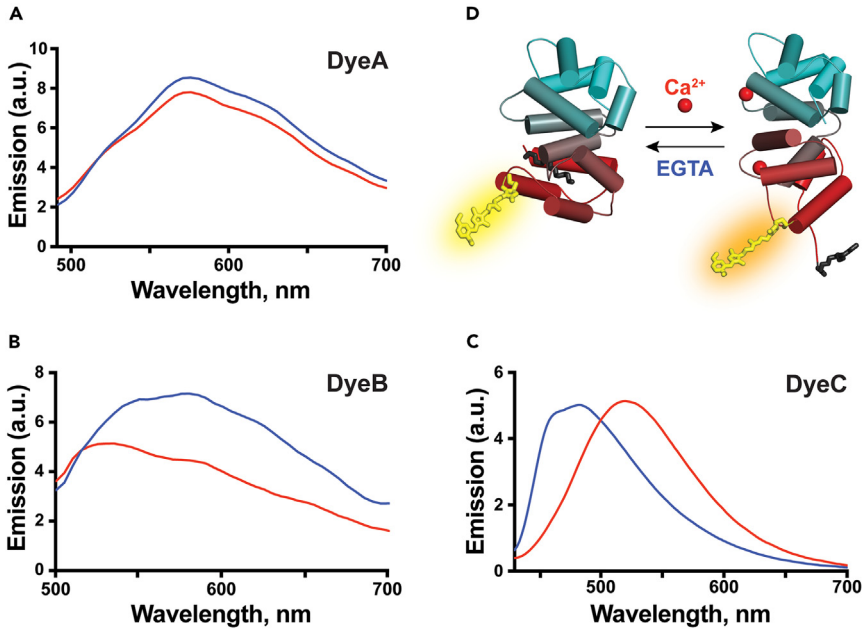

Figure 2. Ca^{2+}-induced conformational and spectral changes of Rec labeled with DyeA, DyeB, and DyeC

(A–C) The Ca^{2+}-induced response of Rec with three BDI-derived labels (DyeA, DyeB, and DyeC). Blue curves correspond to samples in the presence of 100 μM $CaCl_2$, and red curves correspond to calcium-free samples with 100 μM of chelator EGTA. The protein concentration was maintained at 10 μM. Excitation wavelengths were 440 nm, 460 nm, and 410 nm for DyeA, DyeB, and DyeC, respectively.

(D) Structural rearrangements of labeled Rec induced by calcium ions. The structures of the calcium-free and calcium-bound forms are based on PDB IDs 1IKU and 1JSA, respectively.[51,53] DyeC attached to the single native cysteine (C39) in Rec is shown in yellow, and the myristoyl group at the N terminus of Rec is shown in black. Rec is colored in a gradient from red on its N terminus to cyan on the C terminus.

As a negative control for labeling specificity, we also tried labeling $A_{2A}AR_{WT}$ with DyeC. The $A_{2A}AR_{WT}$-DyeC sample showed a very low but detectable fluorescence signal indicating a small percentage of non-specific labeling (<10%, Figure S1B). However, the fluorescence emission spectrum of $A_{2A}AR_{WT}$-DyeC did not change upon the addition of $A_{2A}AR$ ligands (Figure S1D), and, therefore, we concluded that the non-specifically labeled $A_{2A}AR$ did not contribute to the observed spectral changes described in the following.

To test the response of DyeC to $A_{2A}AR$ activation, we measured its fluorescence emission spectra (Figure 3B) in the apo state, as well as in complex with two agonists (NECA and adenosine) and two antagonists (ZM241385 and SCH58261). The $A_{2A}AR$-DyeC emission spectra showed a similar response to both agonists, while the antagonists did not change the emission spectra compared to the apo state. The agonists increased the integrated fluorescence intensity by ~20%, which we quantified as the integrated fluorescence intensity of the emission spectrum (Figure 3C). Furthermore, the agonists induced a red shift of ~5 nm in the emission maximum and resulted in a steeper left shoulder in the spectrum. To quantify this change, we used the ratio between the intensities of the main emission peak at 520 nm and the blue-shifted shoulder peak at 460 nm (I_{520}/I_{460}). The ratio I_{520}/I_{460} changed from ~1.7 for the apo and antagonist-bound receptor to ~2.0 for the agonist-bound receptor (Table S2). Thus, DyeC allowed tracking of the conformation changes in $A_{2A}AR$ based on changes in both the fluorescence intensity and the shape of the spectrum.

To test whether ligand-induced changes in $A_{2A}AR_{L225C}$-DyeC fluorescence spectra were due to conformational changes of the receptor and not due to direct interactions between DyeC and ligands, we conducted displacement experiments of agonist NECA with the excess of antagonist ZM241385, and vice versa (Figure S2). NECA and ZM241385 are both highly specific orthosteric $A_{2A}AR$ ligands (with nanomolar K_d's[63]). The fact that the effect of NECA can be fully reversed by an excess of ZM241385, and vice versa, indicates that both ligands can displace each other from the orthosteric site and have no direct interactions with DyeC.

After establishing the response to orthosteric agonists and antagonists, we used $A_{2A}AR_{L225C}$-DyeC to characterize structural changes in $A_{2A}AR$ induced by one of the most potent allosteric ligands, 5-(N,N-hexamethylene)-amiloride (HMA, Figure 3B). Previous docking simulations suggested that HMA binds to a conserved intramembrane sodium-binding site that is spatially distinct from the orthosteric binding site in $A_{2A}AR$, where all other ligands used in this study bind.[64] Previous functional studies showed that HMA increases the dissociation rate (k_{off}) for $A_{2A}AR$ antagonists, but not agonists.[65,66] At the same time, HMA was shown to displace both antagonists and agonists in competition assays.[64,65,67] In our experiments, the shape of the fluorescence emission spectrum for the $A_{2A}AR_{L225C}$-DyeC complex with HMA differed significantly from that for the receptor bound to other orthosteric ligands used in this study. The emission spectrum in the presence of HMA showed a higher relative intensity of the blue-shifted shoulder peak at 460 nm than the spectra recorded in the presence of either agonists or antagonists. The integrated fluorescence intensity measured in the presence of HMA was statistically indistinguishable from that observed for the agonist-bound $A_{2A}AR$. These results imply that the allosteric ligand HMA stabilizes a distinct conformation of $A_{2A}AR$, which is different

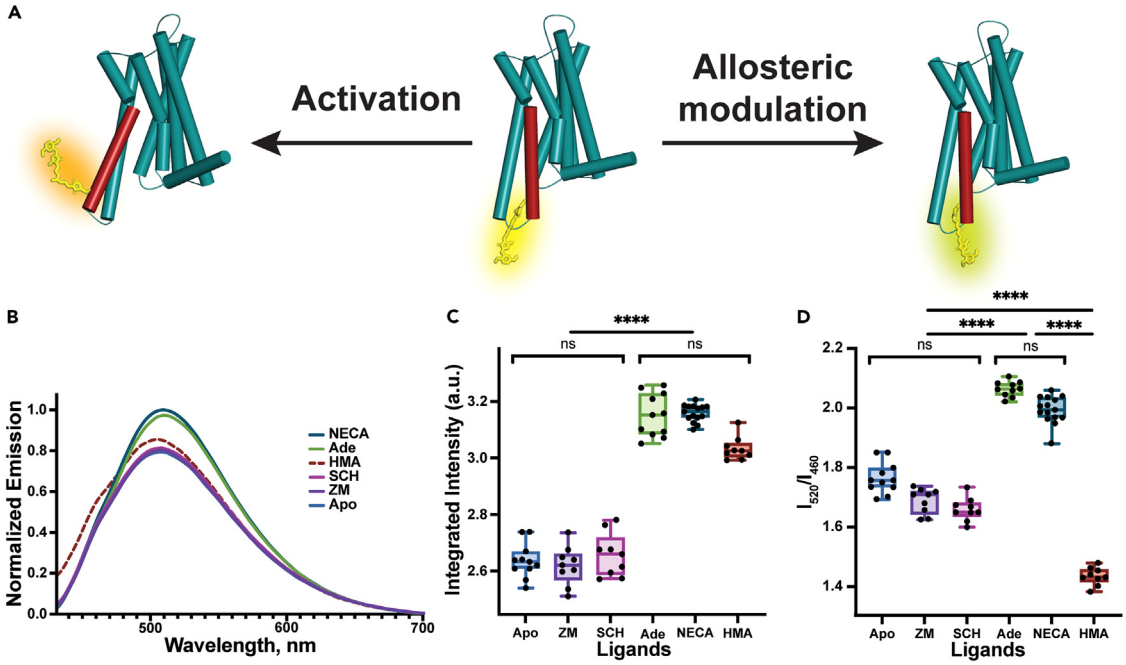

Figure 3. Structural and spectral changes of $A_{2A}AR_{L225C}$-DyeC induced by various ligands

(A) Schematic representation of structural changes caused by agonists and the allosteric modulator HMA in $A_{2A}AR_{L225C}$-DyeC. Structures of the active and inactive $A_{2A}AR$ are sketched from PDB IDs 6GDG and 3RFM, respectively.[45,62] Agonist binding results in an outward shift of the intracellular part of the TM6. The structural effects of the allosteric modulator HMA remain unknown.

(B) Emission spectra of $A_{2A}AR_{L225C}$-DyeC bound to antagonists (ZM241385 and SCH58261), agonists (NECA and adenosine), allosteric modulator (HMA), and in the apo state.

(C) Variation of the integrated intensity of $A_{2A}AR_{L225C}$-DyeC bound to different ligands. The integrated intensity is quantified as the area under the fluorescence emission spectrum from 430 to 700 nm.

(D) Variation of the intensity ratio I_{520}/I_{460} for different ligands. Each condition in C and D was measured at least 9 times with protein from at least three independent purifications; each protein sample was mixed with the ligand independently. The data represent the mean ± SD. The protein concentration was maintained at 10 μM; all ligands were added at a saturating concentration of 100 μM. The significance level is given according to the ordinary one-way ANOVA with the *post hoc* Tukey HSD test: $^{**}p < 0.005$, $^{*}p < 0.05$, ns, not significant..

from the conformations of both inactive apo or antagonist-bound $A_{2A}AR$ and active agonist-bound $A_{2A}AR$. Thus, we demonstrated that the employment of the $A_{2A}AR_{L225C}$-DyeC fluorescent sensor can report on conformational changes induced by $A_{2A}AR$ ligands with different modes of action.

DyeC outperforms other dyes for the detection of conformational changes in $A_{2A}AR$

Bimane is the most commonly used dye for detecting GPCR structural changes (Table S3), while cyanine and certain rhodamine dyes are recognized for their environmental sensitivity and have previously demonstrated responsiveness to GPCR activation.[68–73] Here, we have compared the performance of DyeC with four environmentally sensitive dyes: two cyanine dyes (Cy3 and sulfo-Cy5), rhodamine dye (tetramethylrhodamine-5, TMR-5), and bimane (monobromobimane). Similarly to DyeC, we labeled $A_{2A}AR_{L225C}$ in crude membranes, purified, and reconstituted it in ND. The labeling efficiency was estimated as ~40%, ~25%, ~30%, and ~66% for $A_{2A}AR_{L225C}$ with sulfo-Cy5, Cy3, TMR-5, and bimane, respectively (Figure S1C). The ability of the labeled receptors to bind agonist and antagonist was confirmed via the low-volume differential scanning fluorimetry nanoDSF assay[74] (Figures S3A–S3D). However, the fluorescence emission spectra of sulfo-Cy5, Cy3, and TMR-5, attached to $A_{2A}AR_{L225C}$, showed no response to the addition of the $A_{2A}AR$ ligands (Figures S4A–S4C). Meanwhile, bimane showed ~7% decrease in the integrated intensity (~10% decrease in the emission intensity) and no spectral shift after the addition of the $A_{2A}AR$ agonist (Figure S4D).

MD simulations of $A_{2A}AR_{L225C}$-DyeC reveal the behavior of the label during receptor activation

The most pronounced conformational change in $A_{2A}AR$ upon activation by agonists is a substantial outward displacement of the intracellular segment of TM6.[56] Given that DyeC is located within this region of the protein, we attribute the increase in fluorescence intensity and the redshift in emission maximum caused by agonists to the activated conformation of TM6. In order to rationalize fluorescence changes observed upon $A_{2A}AR$ activation, we conducted MD simulations of $A_{2A}AR_{L225C}$-DyeC embedded in a lipid membrane in both the active

and inactive receptor states. Since obtaining adequate structural ensembles of labeled conformers in unbiased MD simulations still represents a serious computational challenge,[75] which is additionally complicated by the presence of a lipid bilayer, we employed an efficient enhanced sampling technique, known as metadynamics.[76,77] This approach allowed us to estimate free-energy surfaces of DyeC attached to $A_{2A}AR_{L225C}$ and predict its preferred spatial positions in the active and inactive states of the receptor.

The estimated free-energy surfaces revealed a remarkable difference in the predominant orientation of DyeC between the active and inactive conformations of $A_{2A}AR$ (Figures 4A and 4B). In the active state, regions with low free energy values were observed near the protein-lipid interface, where DyeC appears plunged into lipid headgroups. In contrast, the low-free-energy regions in the inactive state were located at the receptor surface, where the label is located in the vicinity of intracellular tips of protein helices remaining largely in the aqueous environment.

We further conducted unbiased molecular simulations without applying any external forces to evaluate the mobility of the DyeC label in the uncovered free-energy minima for both active and inactive receptor states. The dynamics of DyeC is slower when the receptor is in the active conformation, as indicated by higher values of the autocorrelation function (ACF) calculated for the vector describing the dye orientation (Figure 4E). In the $A_{2A}AR$ active conformation, DyeC is immersed in the lipid head group region or trapped between TM5 and TM6 helices, while in the inactive receptor, DyeC is more exposed to the solvent (see Figures 4C and 4D).

These MD results enabled us to propose a mechanistic explanation for the changes in the spectral properties observed upon $A_{2A}AR$ activation. Upon receptor activation, DyeC moves from an aqueous environment in the inactive state to the head group region of the lipid bilayer in the active state (compare Figures 4A and 4B). This region has higher polarity due to the presence of charged phosphate and choline groups. This change in the dye environment may be the reason for the red shift of the fluorescence emission maximum, which is consistent with the observed dependence of the DyeC emission maximum on the solvent logP (Figure 4F, compared with the consensus logP prediction = −2.65 obtained using the SwissADME service[80] for the zwitterionic phosphocholine molecule mimicking the POPC head group). Additionally, in the active state, DyeC experiences greater confinement due to its encapsulation into the G-protein-binding cavity or interaction with TM6 (compare Figures 4D and 4C), resulting in lower ACF values (Figure 4E). This confinement invokes a restriction of the intramolecular rotation (RIR) of DyeC, a phenomenon known to enhance FQY in GFP-derived chromophores.[81] A concomitant increase in fluorescence intensity could also be induced by the higher viscosity of the surrounding lipid environment, which can be up to 5 orders of magnitude greater than that of bulk water,[82–84] further promoting RIR.

DISCUSSION

In this study we utilized solvatochromic dyes inspired by the GFP chromophore to label Rec and $A_{2A}AR$ and measured their responses to ligands. Two out of four dyes (DyeB and DyeC) exhibited Ca^{2+}-dependent changes in their emission spectra when attached to the native C39 of Rec. Considering the structural similarity between Rec and other neuronal calcium sensors, DyeB and DyeC can be implemented for monitoring conformational changes of these proteins, including those involved in cardiac arrhythmia; Alzheimer's, Parkinson's, and Huntington's diseases; and proliferation of cancer cells.[85] DyeC showed the most significant spectral change and was selected for $A_{2A}AR$ labeling. We specifically attached DyeC to the intracellular tip of TM6 of $A_{2A}AR$ containing a single point mutation ($L225^{6.27}C$) using a crude-membrane-labeling procedure. We embedded the labeled $A_{2A}AR$ into ND to mimic a membrane-like environment. These measures improved the structural integrity of the receptor and minimized potential artifacts. Overall, our approach compared favorably with previously reported methods involving environmentally sensitive dyes (Table S3), where receptors were extensively mutated (up to six point mutations) or/and solubilized in detergents.

$A_{2A}AR_{L225C}$-DyeC exhibited a 20% increase in the integrated fluorescence intensity and a 5-nm redshift in the fluorescence emission maximum in response to the interaction with full agonists (NECA and adenosine) but showed no response to the interaction with antagonists (ZM241385 and SCH58261). Both the integrated fluorescence intensity and the I_{520}/I_{460} ratio can be effectively used for quantitative description of the observed spectral changes. The latter ratiometric approach has the advantage that the readout does not depend on the receptor concentration. It can be also useful when analyzing the effects of allosteric ligands, such as HMA, which has a unique impact on the shape of the DyeC fluorescence spectra and can be distinguished from that caused by agonists. These spectral effects can be distinguished through ratiometric analysis but not by integrated fluorescence intensity. The distinctive shape of the emission spectrum implies that structural changes in $A_{2A}AR$ induced by HMA differ from those caused by orthosteric agonists. This finding aligns with a previous NMR study,[43] which showed that HMA increases the population of a state distinct from those stabilized by NECA.

Significantly, all measurements were performed using a microvolumes plate reader, yet they still yielded statistically significant results. Therefore, GFP-inspired dyes hold significant potential in the development of high-throughput ligand-screening methods for both allosteric and orthosteric ligands of GPCRs. Meanwhile, the usage of DyeC may be limited due to two main factors. Firstly, DyeC has low brightness, which imposes requirements on the protein amount. Secondly, its blue excitation wavelength may create additional challenges, particularly for *in vivo* applications.

In terms of the magnitude of agonist-induced changes in the fluorescence intensity and the emission maximum wavelength, DyeC is competitive to other environmentally sensitive labels that have been previously employed to monitor GPCR activation (Table S3). Previous GPCR activation studies using fluorescent labels have been predominantly focused on the β_2-adrenergic receptor (β_2AR) that exhibits agonist-induced structural changes similar to $A_{2A}AR$.[86] Dyes of diverse chemical compositions and properties have been employed to label β_2AR at positions analogous or proximate to the labeling site at the intracellular tip of TM6 used in our study. We experimentally compared DyeC with several selected dyes: cyanine dyes (Cy3 and sulfo-Cy5), commonly known as environment-sensitive dyes, and a rhodamine dye

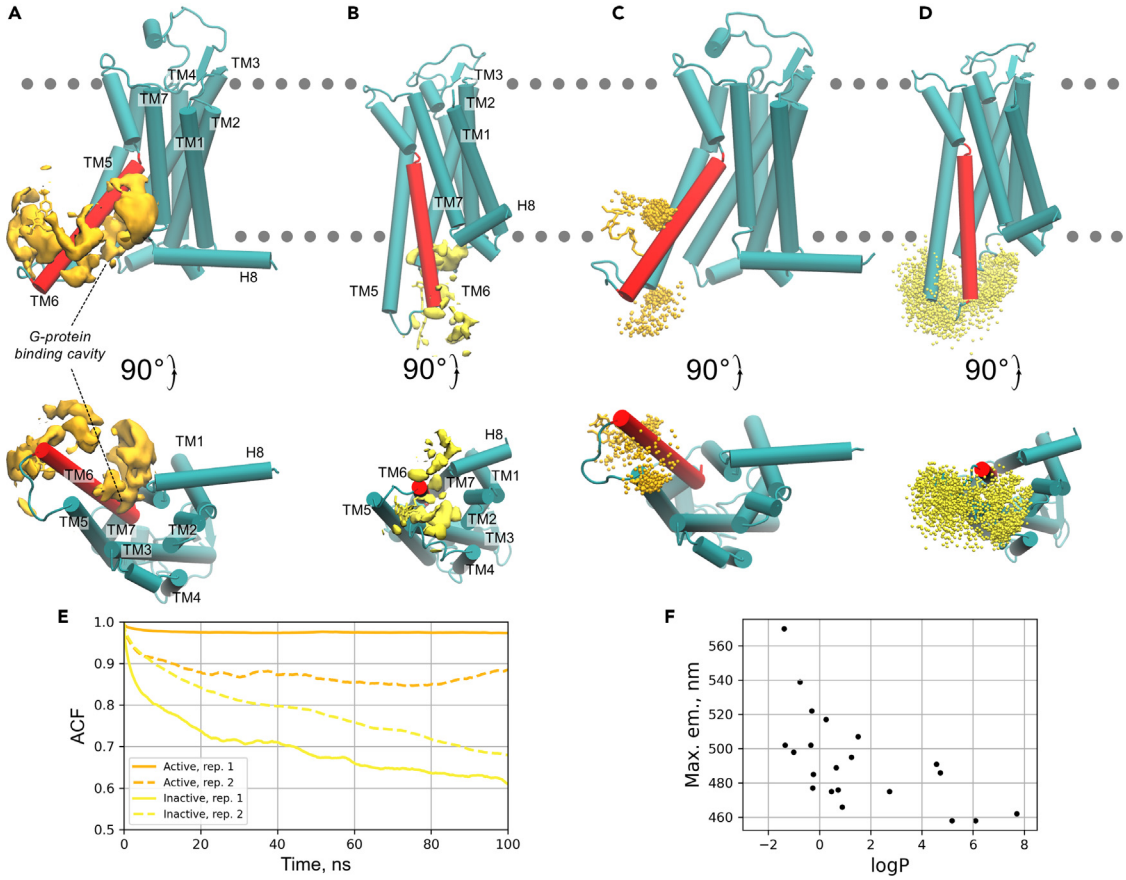

Figure 4. Molecular dynamics simulations of $A_{2A}AR_{L225C}$-DyeC

(A and B) Isosurfaces (yellow) delineate the low-free-energy regions (at +25 kJ/mol level relative to the global free energy minimum) explored by the proximal carbon atom of the dimethoxybenzene ring of DyeC label in the active (A) and inactive (B) states in metadynamics simulations. The $A_{2A}AR_{L225C}$ helices are labeled from TM1 to H8 (TM6 is colored in red), the G-protein binding site is labeled in the active state.

(C and D) Positions of the dimethoxybenzene ring of the DyeC label in the active (C) and inactive (D) complexes throughout the unbiased (i.e., without any external forces applied) MD simulations shown every 0.1 ns as orange/yellow dots, respectively. Each system was simulated for 1,000 ns in two replicates. The positions of the lipid head groups are schematically indicated by the gray dotted line.

(E) Autocorrelation functions (ACFs) calculated for a vector describing the DyeC label position in the unbiased simulations shown in (C) and (D). Higher values of ACF suggest slower reorientational dynamics of the label. Results for two replicates in the active/inactive states are shown in orange/yellow.

(F) Correlation between fluorescence emission maximum of DyeC in different solvents and their partition coefficient, logP. The logP values were obtained from the PubChem/Chemeo databases[78,79] and provided in Table S1. The inverse correlation implies that the translocation of DyeC into the region of the polar head groups of lipids, as observed in the simulations of the active state, leads to a red shift in the fluorescence emission maximum.

(TMR-5) – the brightest dyes (with $\varepsilon > 100\ M^{-1}\cdot cm^{-1}\cdot 10^3$) showed the greatest ligand-induced changes in fluorescence for the β_2AR (~20-~60%), and bimane—the most used dye for β_2AR—showed a 50% intensity change and a 15-nm spectral shift in the presence of agonists (Table S3). For A_{2A}AR labeled at a similarly located cysteine, Cy3, sulfo-Cy5, and TMR-5 showed no ligand-induced changes in fluorescence. Bimane exhibited ~10% change in fluorescence intensity with no spectral shift, while DyeC showed a change of ~20% in intensity and a 5-nm spectral shift (Figure S4). Additionally, bimane has an emission spectrum with the maximum at a shorter wavelength (~450 nm compared to 515 nm for DyeC) and a lower extinction coefficient (~5,000 $M^{-1}cm^{-1}$ [Manglik et al[87]] compared to 14,000 $M^{-1}cm^{-1}$ for DyeC). Thus, in the case of A_{2A}AR, DyeC not only surpasses other dyes but also exhibits a redshifted spectrum and a higher extinction coefficient compared to the next best dye, rendering it a more preferable option for GPCR labeling in certain applications.

The notable differences in behavior between the labels attached to A_{2A}AR in this study and previous findings on β_2AR may stem from various sources, warranting further experimental exploration. One plausible explanation is the use of different membrane-mimicking systems across studies, which can influence receptor activation. Additionally, the activation mechanisms of these two receptors may have inherent differences, as elucidated by NMR studies.[43,88] While the apo form of β_2AR appeared to remain fully inactive, with activated states emerging only upon agonist introduction, active states were already observed in the apo form of A_{2A}AR, with agonist addition amplifying their fraction. This difference in receptor activation may reduce the fluorescence contrast between the apo and agonist-bound forms in the case of A_{2A}AR.

Consequently, while cyanine and rhodamine dyes demonstrated efficacy with β_2AR in previous studies, they did not respond to agonist-induced activation of A_{2A}AR in this work, and bimane showed lower change in fluorescence intensity.

Cy3 attached to the intracellular tip of TM7 was also previously used to monitor A_{2A}AR activation at a single-molecule level[70] where rare transitions to a short-lived highly fluorescent state were observed in the agonist-bound receptors. Approximately a 15% agonist-induced increase in the integrated fluorescence intensity is expected from the single-molecule data, indicating that conformational changes of TM7 have stronger effect on Cy3 fluorescence than the changes around TM6 utilized in our study. Notably, this quantitative comparison is complicated by the selection bias inherent in single-molecule experiments.

Our MD simulations revealed that the observed changes in the DyeC fluorescence spectrum can be explained by the relocation of the fluorescent label to a more confined conformational space with a more hydrophilic environment upon receptor activation. This effect is caused by the agonist-induced outward movement of the DyeC-labeled intracellular tip of TM6, representing a common feature of the activation mechanism in class A GPCRs.[89] Considering these observations, we propose that our approach could be applied to other GPCRs enabling future research on their conformational dynamics. The specific spectral changes of DyeC upon activation of other GPCRs may be influenced by the unique details of their activation, warranting further experimental investigation to fully understand its performance across different receptors.

Limitations of the study

It can be challenging to identify the exact mechanism responsible for the superior sensitivity of DyeC to the conformational changes in A_{2A}AR due to several influencing factors. Different dyes display distinct mechanisms of fluorogenicity and assume varied poses when attached to a protein, depending on multiple factors such as their charges, hydrophobicities, and properties of the linkers. Previous experiments on high-throughput protein mutagenesis and labeling demonstrated that a dye showing high sensitivity to conformational changes in one labeling position can be outperformed by another, formerly less sensitive dye, when attached to another labeling position.[90]

STAR★METHODS

Detailed methods are provided in the online version of this paper and include the following:

- KEY RESOURCES TABLE
- RESOURCE AVAILABILITY
  - Lead contact
  - Materials availability
  - Data and code availability
- METHODS DETAILS
  - Synthesis of dyes
  - (*Z*)-4-(4-(4-cyanobenzylidene)-2-methyl-5-oxo-4,5-dihydro-1*H*-imidazol-1-yl)butanoic acid (Figure S5B)
  - (*Z*)-4-(4-(2,5-dimethoxybenzylidene)-2-methyl-5-oxo-4,5-dihydro-1*H*-imidazol-1-yl)butanoic acid (DyeC acid, Figure S5C)
  - 4-(4-((*Z*)-4-cyanobenzylidene)-2-((*E*)-styryl)-5-oxo-4,5-dihydro-1*H*-imidazol-1-yl)butanoic acid (DyeA acid, Figure S5E)
  - 4-(4-((*Z*)-4-cyanobenzylidene)-2-((*E*)-4-methoxystyryl)-5-oxo-4,5-dihydro-1*H*-imidazol-1-yl)butanoic acid (DyeB acid, Figure S5F)
  - 4-(4-((*Z*)-2,5-dimethoxybenzylidene)-2-((*E*)-2-(pyridin-4-yl)vinyl)-5-oxo-4,5-dihydro-1*H*-imidazol-1-yl)butanoic acid (DyeD acid, Figure S5G)
  - 4-(4-((*Z*)-4-cyanobenzylidene)-2-((*E*)-styryl)-5-oxo-4,5-dihydro-1*H*-imidazol-1-yl)-*N*-(2-(2,5-dioxo-2,5-dihydro-1*H*-pyrrol-1-yl)butanamide (DyeA maleimide, Figure S5I)
  - 4-(4-((*Z*)-4-cyanobenzylidene)-2-((*E*)-4-methoxystyryl)-5-oxo-4,5-dihydro-1*H*-imidazol-1-yl)-N-(2-(2,5-dioxo-2,5-dihydro-1H-pyrrol-1-yl)ethyl)butanamide (DyeB maleimide, Figure S5J)
  - (*Z*)-4-(4-(2,5-dimethoxybenzylidene)-2-methyl-5-oxo-4,5-dihydro-1*H*-imidazol-1-yl)-*N*-(2-(2,5-dioxo-2,5-dihydro-1*H*-pyrrol-1-yl)ethyl) butanamide (DyeC maleimide, Figure S5K)
  - 4-(4-((*Z*)-2,5-dimethoxybenzylidene)-2-((*E*)-2-(pyridin-4-yl)vinyl)-5-oxo-4,5-dihydro-1*H*-imidazol-1-yl)-*N*-(2-(2,5-dioxo-2,5-dihydro-1*H*-pyrrol-1-yl)ethyl)butanamide (DyeD maleimide, Figure S5L)
  - Rec and Rec_{C39D} expression, purification and labeling
  - A_{2A}AR expression, purification, and labeling
  - Free dye absorption and emission measurements
  - Absorption and emission measurements of labeled proteins
  - Molecular dynamics simulations
- QUANTIFICATION AND STATISTICAL ANALYSIS
  - Analysis of the integrated intensities and I_{520}/I_{460}

SUPPLEMENTAL INFORMATION

Supplemental information can be found online at https://doi.org/10.1016/j.isci.2024.110466.

ACKNOWLEDGMENTS

J. Hofkens acknowledges support from the Flemish Government through long-term structural funding Methusalem (CASAS2, Meth/15/04). Functional tests were supported by RSCF research grant 22-74-10036 (to Alx.Mishin.). Structural analysis was supported by RMSHE (grant no. 075-15-2021-1354, to V.B.). A. Belousov, P.Kuzmichev., and A. Bogorodskiy acknowledge support from RMSHE (agreement # 075-03-2024-117, project FSMG-2024-0012). P.O. is a member of an innovative drug development team based on structural biology and bioinformatics at Shenzhen MSU-BIT University #2022KCXTD034 supporting computational simulations.

AUTHOR CONTRIBUTIONS

N.B., V.M., and S.K. synthesized the dyes and measured their optical and NMR spectra under the supervision of Alxr. Mishin, M.B., and K.M. D.Z. expressed and purified Rec under the supervision of E.Z. A. Belousov and P. Khorn expressed, purified, and reconstituted A_{2A}AR in NDs under the supervision of P. Kuzmichev and Alx. Mishin. A. Belousov, I.M., and A. Bogorodskiy labeled Rec and A_{2A}AR and measured and analyzed absorption and fluorescence spectra of the labeled proteins under the supervision of T.G. and V.B. P.O. performed and analyzed MD simulations. A. Belousov, I.M., P.O., and V.B. prepared the draft of the manuscript. A. Belousov, M.B., Alx. Mishin, I.M., and V.B. conceived the study. A. Belousov, I.M., P.O., E.Z., V.I., S.P., J. Hofkens, J. Hendrix, V.C., T.G., M.B., and V.B. discussed the data and analysis and contributed to writing the manuscript. V.B. supervised the work. All the authors contributed to analyzing the data and editing the manuscript.

DECLARATION OF INTERESTS

The authors declare no competing interests.

Received: February 12, 2024
Revised: May 15, 2024
Accepted: July 2, 2024
Published: July 4, 2024

REFERENCES

1. Zimmer, M. (2002). Green fluorescent protein (GFP): applications, structure, and related photophysical behavior. Chem. Rev. *102*, 759–781.
2. Walker, C.L., Lukyanov, K.A., Yampolsky, I.V., Mishin, A.S., Bommarius, A.S., Duraj-Thatte, A.M., Azizi, B., Tolbert, L.M., and Solntsev, K.M. (2015). Fluorescence imaging using synthetic GFP chromophores. Curr. Opin. Chem. Biol. *27*, 64–74.
3. Smirnov, A.Y., Perfilov, M.M., Zaitseva, E.R., Zagudaylova, M.B., Zaitseva, S.O., Mishin, A.S., and Baranov, M.S. (2020). Design of red-shifted and environment-sensitive fluorogens based on GFP chromophore core. Dyes Pigm. *177*, 108258.
4. Ermakova, Y.G., Sen, T., Bogdanova, Y.A., Smirnov, A.Y., Baleeva, N.S., Krylov, A.I., and Baranov, M.S. (2018). Pyridinium Analogues of Green Fluorescent Protein Chromophore: Fluorogenic Dyes with Large Solvent-Dependent Stokes Shift. J. Phys. Chem. Lett. *9*, 1958–1963.
5. Perfilov, M.M., Zaitseva, E.R., Smirnov, A.Y., Mikhaylov, A.A., Baleeva, N.S., Myasnyanko, I.N., Mishin, A.S., and Baranov, M.S. (2022). Environment-sensitive fluorogens based on a GFP chromophore structural motif. Dyes Pigm. *198*, 110033.
6. Lee, J.-S., Baldridge, A., Feng, S., SiQiang, Y., Kim, Y.K., Tolbert, L.M., and Chang, Y.-T. (2011). Fluorescence response profiling for small molecule sensors utilizing the Green fluorescent protein chromophore and its derivatives. ACS Comb. Sci. *13*, 32–38.
7. Zheng, Y., Li, G., Deng, H., Su, Y., Liu, J., and Zhu, X. (2014). Temperature-induced fluorescence enhancement of GFP chromophore containing copolymers for detection of Bacillus thermophilus. Polym. Chem. *5*, 2521–2529.
8. Ruan, N., Yu, X., Li, H., Wang, Y., and Huang, C. (2022). A HBDI-based fluorescent probe for labeling endoplasmic reticulum in living cells. Chem. Asian J. *17*, e202200383. https://doi.org/10.1002/asia.202200383.
9. Wei, X., Zhu, Y., Yu, X., Cai, L., Ruan, N., Wu, L., Jia, N., James, T.D., and Huang, C. (2022). An endoplasmic reticulum targeting green fluorescent protein chromophore-based probe for the detection of viscosity. Chem. Commun. (Camb.) *58*, 10727–10730.
10. Ermakova, Y.G., Bogdanova, Y.A., Baleeva, N.S., Zaitseva, S.O., Guglya, E.B., Smirnov, A.Y., Zagudaylova, M.B., and Baranov, M.S. (2019). Pyridine analogue of fluorescent protein chromophore: Fluorogenic dye suitable for mitochondria staining. Dyes Pigm. *170*, 107550.
11. Cai, L., Li, H., Yu, X., Wu, L., Wei, X., James, T.D., and Huang, C. (2021). Green fluorescent protein GFP-chromophore-based probe for the detection of mitochondrial viscosity in living cells. ACS Appl. Bio Mater. *4*, 2128–2134.
12. Zhi, X., Xiang, W., and Qian, Y. (2021). Modulation of fluorescent protein chromophore for photodynamic therapy and two-photon fluorescent imaging in living cells. J. Lumin. *240*, 118424.
13. Paige, J.S., Wu, K.Y., and Jaffrey, S.R. (2011). RNA mimics of green fluorescent protein. Science *333*, 642–646.
14. Höfer, K., Langejürgen, L.V., and Jäschke, A. (2013). Universal aptamer-based real-time monitoring of enzymatic RNA synthesis. J. Am. Chem. Soc. *135*, 13692–13694.
15. Strack, R.L., Song, W., and Jaffrey, S.R. (2014). Using Spinach-based sensors for fluorescence imaging of intracellular metabolites and proteins in living bacteria. Nat. Protoc. *9*, 146–155.
16. Liu, Y., Wolstenholme, C.H., Carter, G.C., Liu, H., Hu, H., Grainger, L.S., Miao, K., Fares, M., Hoelzel, C.A., Yennawar, H.P., et al. (2018). Modulation of fluorescent protein chromophores to detect protein aggregation with turn-on fluorescence. J. Am. Chem. Soc. *140*, 7381–7384.
17. Meinild, A.-K., Hirayama, B.A., Wright, E.M., and Loo, D.D.F. (2002). Fluorescence studies of ligand-induced conformational changes of the Na(+)/glucose cotransporter. Biochemistry *41*, 1250–1258.
18. Hibbs, R.E., Talley, T.T., and Taylor, P. (2004). Acrylodan-conjugated cysteine side chains reveal conformational state and ligand site locations of the acetylcholine-binding protein. J. Biol. Chem. *279*, 28483–28491.
19. Gensch, T., Komolov, K.E., Senin, I.I., Philippov, P.P., and Koch, K.-W. (2007). Ca2+-dependent conformational changes in the neuronal Ca2+-sensor recoverin probed by the fluorescent dye Alexa647. Proteins *66*, 492–499.
20. Schauer-Vukasinovic, V., Cullen, L., and Daunert, S. (1997). Rational design of a calcium sensing system based on induced conformational changes of calmodulin. J. Am. Chem. Soc. *119*, 11102–11103.
21. Simard, J.R., Getlik, M., Grütter, C., Schneider, R., Wulfert, S., and Rauh, D. (2010). Fluorophore labeling of the glycine-rich loop as a method of identifying inhibitors that bind to active and inactive kinase conformations. J. Am. Chem. Soc. *132*, 4152–4160.
22. Rasheed, M., Richter, C., Chisty, L.T., Kirkpatrick, J., Blackledge, M., Webb, M.R., and Driscoll, P.C. (2014). Ligand-dependent dynamics of the active-site lid in bacterial dimethylarginine dimethylaminohydrolase. Biochemistry *53*, 1092–1104.

23. Gorraitz, E., Hirayama, B.A., Paz, A., Wright, E.M., and Loo, D.D.F. (2017). Active site voltage clamp fluorometry of the sodium glucose cotransporter hSGLT1. Proc. Natl. Acad. Sci. USA *114*, E9980–E9988.
24. Zeng, H.-H., Thompson, R.B., Maliwal, B.P., Fones, G.R., Moffett, J.W., and Fierke, C.A. (2003). Real-time determination of picomolar free Cu(II) in seawater using a fluorescence-based fiber optic biosensor. Anal. Chem. *75*, 6807–6812.
25. Salins, L.L.E., Goldsmith, E.S., Ensor, C.M., and Daunert, S. (2002). A fluorescence-based sensing system for the environmental monitoring of nickel using the nickel binding protein from Escherichia coli. Anal. Bioanal. Chem. *372*, 174–180.
26. Namiki, S., Sakamoto, H., Iinuma, S., Iino, M., and Hirose, K. (2007). Optical glutamate sensor for spatiotemporal analysis of synaptic transmission. Eur. J. Neurosci. *25*, 2249–2259.
27. Kitajima, N., Takikawa, K., Sekiya, H., Satoh, K., Asanuma, D., Sakamoto, H., Takahashi, S., Hanaoka, K., Urano, Y., Namiki, S., et al. (2020). Real-time in vivo imaging of extracellular ATP in the brain with a hybrid-type fluorescent sensor. Elife *9*, e57544. https://doi.org/10.7554/eLife.57544.
28. Donaldson, T., Iozzino, L., Deacon, L.J., Billones, H., Ausili, A., D'Auria, S., and Dattelbaum, J.D. (2017). Engineering a switch-based biosensor for arginine using a Thermotoga maritima periplasmic binding protein. Anal. Biochem. *525*, 60–66.
29. Goguen, B.N., Loving, G.S., and Imperiali, B. (2011). Development of a fluorogenic sensor for activated Cdc42. Bioorg. Med. Chem. Lett. *21*, 5058–5061.
30. Hauser, A.S., Chavali, S., Masuho, I., Jahn, L.J., Martemyanov, K.A., Gloriam, D.E., and Babu, M.M. (2018). Pharmacogenomics of GPCR Drug Targets. Cell *172*, 41–54.e19.
31. Cristalli, G., Lambertucci, C., Marucci, G., Volpini, R., and Dal Ben, D. (2008). A2A adenosine receptor and its modulators: overview on a druggable GPCR and on structure-activity relationship analysis and binding requirements of agonists and antagonists. Curr. Pharm. Des. *14*, 1525–1552.
32. Wootten, D., Christopoulos, A., and Sexton, P.M. (2013). Emerging paradigms in GPCR allostery: implications for drug discovery. Nat. Rev. Drug Discov. *12*, 630–644.
33. Conn, P.J., Christopoulos, A., and Lindsley, C.W. (2009). Allosteric modulators of GPCRs: a novel approach for the treatment of CNS disorders. Nat. Rev. Drug Discov. *8*, 41–54.
34. Keov, P., Sexton, P.M., and Christopoulos, A. (2011). Allosteric modulation of G protein-coupled receptors: a pharmacological perspective. Neuropharmacology *60*, 24–35.
35. May, L.T., Leach, K., Sexton, P.M., and Christopoulos, A. (2007). Allosteric modulation of G protein-coupled receptors. Annu. Rev. Pharmacol. Toxicol. *47*, 1–51.
36. Slosky, L.M., Caron, M.G., and Barak, L.S. (2021). Biased Allosteric Modulators: New Frontiers in GPCR Drug Discovery. Trends Pharmacol. Sci. *42*, 283–299.
37. Conn, P.J., Lindsley, C.W., Meiler, J., and Niswender, C.M. (2014). Opportunities and challenges in the discovery of allosteric modulators of GPCRs for treating CNS disorders. Nat. Rev. Drug Discov. *13*, 692–708.
38. Christopoulos, A., and Kenakin, T. (2002). G protein-coupled receptor allosterism and complexing. Pharmacol. Rev. *54*, 323–374.
39. Chen, J.-F., Eltzschig, H.K., and Fredholm, B.B. (2013). Adenosine receptors as drug targets–what are the challenges? Nat. Rev. Drug Discov. *12*, 265–286.
40. Ohta, A., and Sitkovsky, M. (2001). Role of G-protein-coupled adenosine receptors in downregulation of inflammation and protection from tissue damage. Nature *414*, 916–920.
41. Morelli, M., Di Paolo, T., Wardas, J., Calon, F., Xiao, D., and Schwarzschild, M.A. (2007). Role of adenosine A2A receptors in parkinsonian motor impairment and l-DOPA-induced motor complications. Prog. Neurobiol. *83*, 293–309.
42. Jaakola, V.-P., Griffith, M.T., Hanson, M.A., Cherezov, V., Chien, E.Y.T., Lane, J.R., Ijzerman, A.P., and Stevens, R.C. (2008). The 2.6 angstrom crystal structure of a human A2A adenosine receptor bound to an antagonist. Science *322*, 1211–1217.
43. Ye, L., Van Eps, N., Zimmer, M., Ernst, O.P., and Prosser, R.S. (2016). Activation of the A2A adenosine G-protein-coupled receptor by conformational selection. Nature *533*, 265–268.
44. Weinert, T., Olieric, N., Cheng, R., Brünle, S., James, D., Ozerov, D., Gashi, D., Vera, L., Marsh, M., Jaeger, K., et al. (2017). Serial millisecond crystallography for routine room-temperature structure determination at synchrotrons. Nat. Commun. *8*, 542.
45. García-Nafría, J., Lee, Y., Bai, X., Carpenter, B., and Tate, C.G. (2018). Cryo-EM structure of the adenosine A receptor coupled to an engineered heterotrimeric G protein. Elife *7*, e35946. https://doi.org/10.7554/eLife.35946.
46. Yen, H.-Y., Hoi, K.K., Liko, I., Hedger, G., Horrell, M.R., Song, W., Wu, D., Heine, P., Warne, T., Lee, Y., et al. (2018). PtdIns(4,5)P_2 stabilizes active states of GPCRs and enhances selectivity of G-protein coupling. Nature *559*, 423–427.
47. Lee, C.-Y., Chen, Y.-C., Lin, H.-C., Jhong, Y., Chang, C.-W., Tsai, C.-H., Kao, C.-L., and Chien, T.-C. (2012). Facile synthesis of 4-arylidene-5-imidazolinones as synthetic analogs of fluorescent protein chromophore. Tetrahedron *68*, 5898–5907.
48. Deng, H., Yu, C., Gong, L., and Zhu, X. (2016). Self-Restricted Green Fluorescent Protein Chromophore Analogues: Dramatic Emission Enhancement and Remarkable Solvatofluorochromism. J. Phys. Chem. Lett. *7*, 2935–2944.
49. Burgoyne, R.D. (2007). Neuronal calcium sensor proteins: generating diversity in neuronal Ca2+ signalling. Nat. Rev. Neurosci. *8*, 182–193.
50. Zang, J., and Neuhauss, S.C.F. (2018). The Binding Properties and Physiological Functions of Recoverin. Front. Mol. Neurosci. *11*, 473.
51. Ames, J.B., Ishima, R., Tanaka, T., Gordon, J.I., Stryer, L., and Ikura, M. (1997). Molecular mechanics of calcium-myristoyl switches. Nature *389*, 198–202.
52. Timr, Š., Kadlec, J., Srb, P., Ollila, O.H.S., and Jungwirth, P. (2018). Calcium Sensing by Recoverin: Effect of Protein Conformation on Ion Affinity. J. Phys. Chem. Lett. *9*, 1613–1619.
53. Tanaka, T., Ames, J.B., Harvey, T.S., Stryer, L., and Ikura, M. (1995). Sequestration of the membrane-targeting myristoyl group of recoverin in the calcium-free state. Nature *376*, 444–447.
54. Ballesteros, J.A., and Weinstein, H. (1995). [19] Integrated methods for the construction of three-dimensional models and computational probing of structure-function relations in G protein-coupled receptors. In Methods in Neurosciences Methods in neurosciences (Elsevier), pp. 366–428.
55. Fredriksson, R., Lagerström, M.C., Lundin, L.-G., and Schiöth, H.B. (2003). The G-protein-coupled receptors in the human genome form five main families. Phylogenetic analysis, paralogon groups, and fingerprints. Mol. Pharmacol. *63*, 1256–1272.
56. Xu, F., Wu, H., Katritch, V., Han, G.W., Jacobson, K.A., Gao, Z.-G., Cherezov, V., and Stevens, R.C. (2011). Structure of an agonist-bound human A2A adenosine receptor. Science *332*, 322–327.
57. Fernandes, D.D., Neale, C., Gomes, G.-N.W., Li, Y., Malik, A., Pandey, A., Orazietti, A.P., Wang, X., Ye, L., Scott Prosser, R., and Gradinaru, C.C. (2021). Ligand modulation of the conformational dynamics of the A_{2A} adenosine receptor revealed by single-molecule fluorescence. Sci. Rep. *11*, 5910.
58. Maslov, I., Volkov, O., Khorn, P., Orekhov, P., Gusach, A., Kuzmichev, P., Gerasimov, A., Luginina, A., Coucke, Q., Bogorodskiy, A., et al. (2023). Sub-millisecond conformational dynamics of the A2A adenosine receptor revealed by single-molecule FRET. Commun. Biol. *6*, 362.
59. Huang, S.K., Pandey, A., Tran, D.P., Villanueva, N.L., Kitao, A., Sunahara, R.K., Sljoka, A., and Prosser, R.S. (2021). Delineating the conformational landscape of the adenosine A_{2A} receptor during G protein coupling. Cell *184*, 1884–1894.e14.
60. Ye, L., Neale, C., Sljoka, A., Lyda, B., Pichugin, D., Tsuchimura, N., Larda, S.T., Pomès, R., García, A.E., Ernst, O.P., et al. (2018). Mechanistic insights into allosteric regulation of the A_{2A} adenosine G protein-coupled receptor by physiological cations. Nat. Commun. *9*, 1372.
61. Sušac, L., O'Connor, C., Stevens, R.C., and Wüthrich, K. (2015). In-Membrane Chemical Modification (IMCM) for Site-Specific Chromophore Labeling of GPCRs. Angew. Chem. Int. Ed. Engl. *54*, 15246–15249.
62. Doré, A.S., Robertson, N., Errey, J.C., Ng, I., Hollenstein, K., Tehan, B., Hurrell, E., Bennett, K., Congreve, M., Magnani, F., et al. (2011). Structure of the adenosine A(2A) receptor in complex with ZM241385 and the xanthines XAC and caffeine. Structure *19*, 1283–1293.
63. Alexander, S.P.H., Christopoulos, A., Davenport, A.P., Kelly, E., Mathie, A.A., Peters, J.A., Veale, E.L., Armstrong, J.F., Faccenda, E., Harding, S.D., et al. (2023). The Concise Guide to PHARMACOLOGY 2023/24: G protein-coupled receptors. Br. J. Pharmacol. *180*, S23–S144. https://doi.org/10.1111/bph.16177.
64. Gutiérrez-de-Terán, H., Massink, A., Rodríguez, D., Liu, W., Han, G.W., Joseph, J.S., Katritch, I., Heitman, L.H., Xia, L., Ijzerman, A.P., et al. (2013). The role of a sodium ion binding site in the allosteric modulation of the A(2A) adenosine G protein-coupled receptor. Structure *21*, 2175–2185.
65. Gao, Z.G., and Ijzerman, A.P. (2000). Allosteric modulation of A(2A) adenosine

receptors by amiloride analogues and sodium ions. Biochem. Pharmacol. *60*, 669–676.
66. Gao, Z.-G., Melman, N., Erdmann, A., Kim, S.G., Müller, C.E., IJzerman, A.P., and Jacobson, K.A. (2003). Differential allosteric modulation by amiloride analogues of agonist and antagonist binding at A(1) and A(3) adenosine receptors. Biochem. Pharmacol. *65*, 525–534.
67. Massink, A., Gutiérrez-de-Terán, H., Lenselink, E.B., Ortiz Zacarías, N.V., Xia, L., Heitman, L.H., Katritch, V., Stevens, R.C., and IJzerman, A.P. (2015). Sodium ion binding pocket mutations and adenosine A2A receptor function. Mol. Pharmacol. *87*, 305–313.
68. Lamichhane, R., Liu, J.J., Pljevaljcic, G., White, K.L., van der Schans, E., Katritch, V., Stevens, R.C., Wüthrich, K., and Millar, D.P. (2015). Single-molecule view of basal activity and activation mechanisms of the G protein-coupled receptor β2AR. Proc. Natl. Acad. Sci. USA *112*, 14254–14259.
69. Lamichhane, R., Liu, J.J., White, K.L., Katritch, V., Stevens, R.C., Wüthrich, K., and Millar, D.P. (2020). Biased Signaling of the G-Protein-Coupled Receptor β2AR Is Governed by Conformational Exchange Kinetics. Structure *28*, 371–377.e3.
70. Wei, S., Thakur, N., Ray, A.P., Jin, B., Obeng, S., McCurdy, C.R., McMahon, L.R., Gutiérrez-de-Terán, H., Eddy, M.T., and Lamichhane, R. (2022). Slow conformational dynamics of the human A2A adenosine receptor are temporally ordered. Structure *30*, 329–337.e5.
71. Neumann, L., Wohland, T., Whelan, R.J., Zare, R.N., and Kobilka, B.K. (2002). Functional immobilization of a ligand-activated G-protein-coupled receptor. Chembiochem *3*, 993–998.
72. Swaminath, G., Xiang, Y., Lee, T.W., Steenhuis, J., Parnot, C., and Kobilka, B.K. (2004). Sequential binding of agonists to the beta2 adrenoceptor. Kinetic evidence for intermediate conformational states. J. Biol. Chem. *279*, 686–691.
73. Swaminath, G., Deupi, X., Lee, T.W., Zhu, W., Thian, F.S., Kobilka, T.S., and Kobilka, B. (2005). Probing the beta2 adrenoceptor binding site with catechol reveals differences in binding and activation by agonists and partial agonists. J. Biol. Chem. *280*, 22165–22171.
74. Cecchetti, C., Strauss, J., Stohrer, C., Naylor, C., Pryor, E., Hobbs, J., Tanley, S., Goldman, A., and Byrne, B. (2021). A novel high-throughput screen for identifying lipids that stabilise membrane proteins in detergent based solution. PLoS One *16*, e0254118.
75. Jeschke, G. (2022). Integration of nanometer-range label-to-label distances and their distributions into modelling approaches. Biomolecules *12*, 1369.
76. Barducci, A., Bonomi, M., and Parrinello, M. (2011). Metadynamics. WIREs Comput. Mol. Sci. *1*, 826–843.
77. Laio, A., and Parrinello, M. (2002). Escaping free-energy minima. Proc. Natl. Acad. Sci. USA *99*, 12562–12566.
78. Kim, S., Chen, J., Cheng, T., Gindulyte, A., He, J., He, S., Li, Q., Shoemaker, B.A., Thiessen, P.A., Yu, B., et al. (2023). PubChem 2023 update. Nucleic Acids Res. *51*, D1373–D1380.
79. Cheméo Cheméo. www.chemeo.com.
80. Daina, A., Michielin, O., and Zoete, V. (2017). SwissADME: a free web tool to evaluate pharmacokinetics, drug-likeness and medicinal chemistry friendliness of small molecules. Sci. Rep. *7*, 42717.
81. Ye, S.(叶松涛), Tang, Y.(唐宇琦), and Zhang, X.(张鑫) (2022). Principles, modulation, and applications of fluorescent protein chromophores. Chem. Phys. Rev. *3*, 011308.
82. Cicuta, P., Keller, S.L., and Veatch, S.L. (2007). Diffusion of liquid domains in lipid bilayer membranes. J. Phys. Chem. B *111*, 3328–3331.
83. Gambin, Y., Lopez-Esparza, R., Reffay, M., Sierecki, E., Gov, N.S., Genest, M., Hodges, R.S., and Urbach, W. (2006). Lateral mobility of proteins in liquid membranes revisited. Proc. Natl. Acad. Sci. USA *103*, 2098–2102.
84. Vaz, W.L.C., Stümpel, J., Hallmann, D., Gambacorta, A., and De Rosa, M. (1987). Bounding fluid viscosity and translational diffusion in a fluid lipid bilayer. Eur. Biophys. J. *15*, 111–115.
85. Burgoyne, R.D., Helassa, N., McCue, H.V., and Haynes, L.P. (2019). Calcium Sensors in Neuronal Function and Dysfunction. Cold Spring Harb. Perspect. Biol. *11*, a035154. https://doi.org/10.1101/cshperspect.a035154.
86. Lebon, G., Warne, T., Edwards, P.C., Bennett, K., Langmead, C.J., Leslie, A.G.W., and Tate, C.G. (2011). Agonist-bound adenosine A2A receptor structures reveal common features of GPCR activation. Nature *474*, 521–525.
87. Bromobimane Sigma-Aldrich. https://www.sigmaaldrich.com/BE/en/product/sial/b4380.
88. Manglik, A., Kim, T.H., Masureel, M., Altenbach, C., Yang, Z., Hilger, D., Lerch, M.T., Kobilka, T.S., Thian, F.S., Hubbell, W.L., et al. (2015). Structural insights into the dynamic process of β2-adrenergic receptor signaling. Cell *162*, 1431.
89. Zhou, Q., Yang, D., Wu, M., Guo, Y., Guo, W., Zhong, L., Cai, X., Dai, A., Jang, W., Shakhnovich, E.I., et al. (2019). Common activation mechanism of class A GPCRs. Elife *8*, e50279. https://doi.org/10.7554/eLife.50279.
90. Takikawa, K., Asanuma, D., Namiki, S., Sakamoto, H., Ariyoshi, T., Kimpara, N., and Hirose, K. (2014). High-throughput development of a hybrid-type fluorescent glutamate sensor for analysis of synaptic transmission. Angew. Chem. Int. Ed. Engl. *53*, 13439–13443.
91. Webb, B., and Sali, A. (2016). Comparative protein structure modeling using MODELLER. Curr. Protoc. Bioinformatics *54*, 5.6.1–5.6.37.
92. Jo, S., Kim, T., Iyer, V.G., and Im, W. (2008). CHARMM-GUI: a web-based graphical user interface for CHARMM. J. Comput. Chem. *29*, 1859–1865.
93. Abraham, M.J., Murtola, T., Schulz, R., Páll, S., Smith, J.C., Hess, B., and Lindahl, E. (2015). GROMACS: High performance molecular simulations through multi-level parallelism from laptops to supercomputers. SoftwareX *1–2*, 19–25.
94. Neese, F. (2018). Software update: the ORCA program system, version 4.0. WIREs Comput. Mol. Sci. *8*, e1327.
95. Orekhov, P. (2024). Monitoring GPCR Conformation with GFP-Inspired Dyes (Mendeley Data). https://doi.org/10.17632/67G48NMRWD.1.
96. Castañar, L., Saurí, J., Williamson, R.T., Virgili, A., and Parella, T. (2014). Pure in-phase heteronuclear correlation NMR experiments. Angew. Chem. Int. Ed. Engl. *53*, 8379–8382.
97. Senin, I.I., Zargarov, A.A., Alekseev, A.M., Gorodovikova, E.N., Lipkin, V.M., and Philippov, P.P. (1995). N-myristoylation of recoverin enhances its efficiency as an inhibitor of rhodopsin kinase. FEBS Lett. *376*, 87–90.
98. Permyakov, S.E., Zernii, E.Y., Knyazeva, E.L., Denesyuk, A.I., Nazipova, A.A., Kolpakova, T.V., Zinchenko, D.V., Philippov, P.P., Permyakov, E.A., and Senin, I.I. (2012). Oxidation mimicking substitution of conservative cysteine in recoverin suppresses its membrane association. Amino Acids *42*, 1435–1442.
99. McLean, M.A., Denisov, I.G., Grinkova, Y.V., and Sligar, S.G. (2020). Dark, Ultra-Dark and Ultra-Bright Nanodiscs for membrane protein investigations. Anal. Biochem. *607*, 113860.
100. Würth, C., Grabolle, M., Pauli, J., Spieles, M., and Resch-Genger, U. (2013). Relative and absolute determination of fluorescence quantum yields of transparent samples. Nat. Protoc. *8*, 1535–1550.
101. Carpenter, B., Nehmé, R., Warne, T., Leslie, A.G.W., and Tate, C.G. (2016). Structure of the adenosine A2A receptor bound to an engineered G protein. Nature *536*, 104–107.
102. Tribello, G.A., Bonomi, M., Branduardi, D., Camilloni, C., and Bussi, G. (2014). PLUMED 2: New feathers for an old bird. Comput. Phys. Commun. *185*, 604–613.
103. Hopkins, C.W., Le Grand, S., Walker, R.C., and Roitberg, A.E. (2015). Long-time-step molecular dynamics through hydrogen mass repartitioning. J. Chem. Theory Comput. *11*, 1864–1874.
104. Hess, B., Bekker, H., Berendsen, H.J.C., and Fraaije, J.G.E. (1997). LINCS: A linear constraint solver for molecular simulations. J. Comp. Chem. *18*, 1463–1472. https://doi.org/10.1002/(sici)1096-987x(199709)18:12<1463::aid-jcc4>3.0.co;2-h.
105. Lindorff-Larsen, K., Piana, S., Palmo, K., Maragakis, P., Klepeis, J.L., Dror, R.O., and Shaw, D.E. (2010). Improved side-chain torsion potentials for the Amber ff99SB protein force field. Proteins *78*, 1950–1958.
106. The Amber Molecular Dynamics Package https://ambermd.org/.
107. Goncharuk, M.V., Baleeva, N.S., Nolde, D.E., Gavrikov, A.S., Mishin, A.V., Mishin, A.S., Sosorev, A.Y., Arseniev, A.S., Goncharuk, S.A., Borshchevskiy, V.I., et al. (2022). Structure-based rational design of an enhanced fluorogen-activating protein for fluorogens based on GFP chromophore. Commun. Biol. *5*, 706.

STAR★METHODS

KEY RESOURCES TABLE

REAGENT or RESOURCE	SOURCE	IDENTIFIER
Bacterial and virus strains		
Escherichia coli strain BL21-CodonPlus®(DE3)-RIL-X	Agilent	Cat# 230265
Chemicals, peptides, and recombinant proteins		
$KMnO_4$	Sigma-Aldrich	Cat# 60470
Myristic acid	Sigma-Aldrich	Cat# 8.00399
isopropyl β-D-1-thiogalactopyranoside	Sigma-Aldrich	Cat# PHG0010
Tris-HCl	Sigma-Aldrich	Cat# T3253
$MgCl_2$	Sigma-Aldrich	Cat# 8.14733
EDTA	Sigma-Aldrich	Cat# 4005-OP
EGTA	Sigma-Aldrich	Cat# 03777
PMSF	Sigma-Aldrich	Cat# PMSF-RO
DTT	Sigma-Aldrich	Cat# D0632
$CaCl_2$	Sigma-Aldrich	Cat# 499609
NaCl	Sigma-Aldrich	Cat# S9888
HEPES	Sigma-Aldrich	Cat# RDD035
DMSO	Sigma-Aldrich	Cat# 472301
X-tremeGENE™ HP DNA Transfection Reagent	Roche	Cat# XTGHP-RO
Transfection Medium	Exression System	Cat# 95-020-020
AEBSF	Gold Biotechnology	Cat# A-540
E-64	Cayman Chemical	Cat# 10007963
Leupeptin	Cayman Chemical	Cat# 14026
KCl	Sigma-Aldrich	Cat# P9541
theophylline	Sigma-Aldrich	Cat# T0800000
sulfo-Cy5 maleimide	Lumiprobe	Cat# 13380
Cy3 maleimide	Lumiprobe	Cat# 11080
TMR-5 maleimide	Lumiprobe	Cat# 17180
monobrombimane	Sigma-Aldrich	Cat# B4380
Glycerol	Sigma-Aldrich	Cat# 356352-M
DDM	Sigma-Aldrich	Cat# D4641
CHS	Sigma-Aldrich	Cat# C6013
Imidazole	Sigma-Aldrich	Cat# I2399
ATP	Sigma-Aldrich	Cat# A26209
POCP	Avanti Polar Lipids	Cat# 850855C
POPG	Avanti Polar Lipids	Cat# 840457P
Ni-NTA Agarose	Qiagen	Cat# 30210
TALON resin	Clontech	Cat# 031716
Bio-Beads SM-2	Biorad	Cat# 1523920
ZM241385	Cayman Chemical	Cat# 20447
NECA	Tocris	Cat# 16-911-0
Adenosine	Tocris	Cat# 36-245-0R

(*Continued on next page*)

Continued

REAGENT or RESOURCE	SOURCE	IDENTIFIER
SCH58261	Tocris	Cat# 22-701-0
HMA	Sigma-Aldrich	Cat# A9561
$CDCl_3$	Sigma-Aldrich	Cat# 151823
DMSO-d_6	Sigma-Aldrich	Cat# 151874
SDS	Sigma-Aldrich	Cat# 436143
DyeA	This article	N/A
DyeB	This article	N/A
DyeC	This article	N/A
DyeD	This article	N/A
Deposited data		
MD custom script	This paper	https://github.com/porekhov/A2a_GFP_core_dyes
Raw data for MD	This paper; Mendeley Data	https://doi.org/10.17632/67G48NMRWD.1
Recombinant DNA		
pFastBac1 vector	Invitrogen	Cat# 10360010
pET11d vector	Novagen	Cat# 69439
Software and algorithms		
Prism v9.4.1	GraphPad	https://www.graphpad.com/
MODELLER	Webb and Sali[91]	
CHARMM-GUI	Jo et al.[92]	
GROMACS	Abraham et al.[93]	
ORCA v4.0	Neese[94]	
AMBER	https://ambermd.org/	
PR.ThermControl software	NanoTemper	
Other		
F_{254} glass-backed plates	Merck	Cat# 105738
700 MHz Bruker Avance NMR	Bruker	N/A
800 MHz Bruker Avance III NMR	Bruker	N/A
SMP 30 apparatus	Stuart Scientific	Cat# SMP30
micrOTOF II instrument	Bruker	N/A
ESI Tuning Mix	Agilent	Cat# G1969-85000
Phenyl Sepharose column	Cytiva	Cat# GE17-1082-01
HiTrap Q FF column	Cytiva	Cat# GE17-5156-01
Luna C18 reversed-phase column	Phenomenex	N/A
10 kDa MWCO Amicon Ultra centrifugal filter unit	Merck Millipore	Cat# UFC8010D
Stirred Cell Model 8003	Millipore	Cat# 5125-M
10 kDa MWCO regenerated cellulose filter	Millipore	Cat# PLGC04710
Breathe-Easy membranes	Greiner BioOne	Cat# Z380059
Shel Lab incubator	Shel Lab	N/A
Innova 44	New Brunswick	N/A
vent-cap flasks	Corning	
BD Accuri C6	BD Biosciences	N/A
30 kDa MWCO Amicon Ultra filter	Merck	Cat# UFC8030
Hei-VAP Ultimate ML/G1	Heidolph	N/A

(*Continued on next page*)

Continued

REAGENT or RESOURCE	SOURCE	IDENTIFIER
Dry Oil-Free Deep Vacuum System	ChemStar®	N/A
100 kDa MWCO Amicon Ultra filter	Merck	Cat# UFC8100
Mini-Protean IV system	Bio-Rad	Cat# 1658000
Prometheus NT.48 capillaries	NanoTemper	Cat# PR-C002
Prometheus NT.48 Nano-DSF instrument	NanoTemper	N/A
Synergy H4	Agilent BioTek	N/A
Take3 Microvolume Plate	Agilent BioTek	Cat# 27671

RESOURCE AVAILABILITY

Lead contact

Further information and requests for resources and reagents should be directed to and will be fulfilled by the lead contact, Valentin Borshchevskiy (borshchesvkiy@gmail.com).

Materials availability

Schemes of synthesis of the DyeA, DyeB, DyeC, and DyeD are available in the methods section.

Data and code availability

- All data reported in this paper will be shared by the lead contact upon request.
- All original code has been deposited at https://github.com/porekhov/A2a_GFP_core_dyes and is publicly available as of the date of publication. The resulting topologies, starting configurations, and trajectories are available in the Mendeley Data.[95] Accession numbers are listed in the key resources table.
- Any additional information required to reanalyze the data reported in this paper is available from the lead contact upon request.

METHODS DETAILS

Synthesis of dyes

Commercially available reagents of highest purity were used without additional purification. Merck Kieselgel 60 was used for flash chromatography. Thin-layer chromatography was performed on silica gel 60 F_{254} glass-backed plates (Merck). Visualization was enabled by staining with $KMnO_4$ and illumination with UV light (254 or 312 nm).

NMR spectra were recorded on a 700 MHz Bruker Avance NMR at 303 K and a 800 MHz Bruker Avance III NMR at 333 K. Chemical shifts are reported relative to the residue peaks of $CDCl_3$ (7.27 ppm for ^1H and 77.0 ppm for ^{13}C) or DMSO-d_6 (2.51 ppm for ^1H and 39.5 ppm for ^{13}C). Melting points were measured on an SMP 30 apparatus (Stuart Scientific). High-resolution mass spectra (HRMS) were recorded on a Bruker micrOTOF II instrument using electrospray ionization (ESI). The measurements were carried out in a positive ion mode (interface capillary voltage - 4500 V) or in a negative ion mode (3200 V); mass range from m/z 50 to m/z 3000; external or internal calibration was done with ESI Tuning Mix (Agilent). A syringe injection was used for solutions in acetonitrile, methanol, or water (flow rate 3 mL/min). Nitrogen was applied as a dry gas; interface temperature was set at 180°C.

Synthetic procedures

Preparation of (Z)-4-(4-benzylidene-2-methyl-5-oxo-4,5-dihydro-1H-imidazol-1-yl)butanoic acids (Figure S5A).

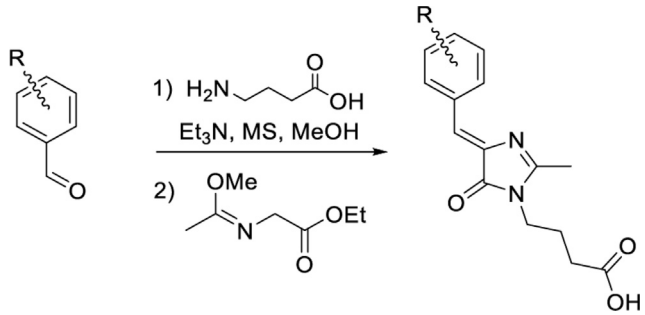

The corresponding aromatic aldehyde (12 mmol) was dissolved in MeOH (50 mL) and mixed with 4-aminobutanoic acid (1.35 g, 13 mmol), triethylamine (2.8 mL, 20 mmol) and MS 4 Å (5 g) and 3 Å (5 g). The mixture was stirred for 5 days at room temperature. The mixture was filtered; MS were washed with MeOH (2 × 10 mL). The solvent was evaporated and ethyl((methoxy)amino)acetate (2.4 g, 15 mmol) was added to the residue. The mixture was stirred for 4 days at room temperature, solvents were evaporated and the product was purified by column chromatography (CH_2Cl_2-iPrOH-AcOH, 100/5/0.5).

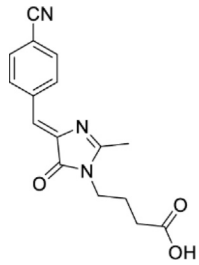

(*Z*)-4-(4-(4-cyanobenzylidene)-2-methyl-5-oxo-4,5-dihydro-1*H*-imidazol-1-yl)butanoic acid (Figure S5B)

Yellow solid (1.92 g, 54%); mp = 176–179°C; ^{1}H NMR (700 MHz, DMSO-d_6) δ ppm 12.10 (br. s., 1 H), 8.38 (d, J = 8.4 Hz, 2 H), 7.90 (d, J = 8.4 Hz, 2 H), 7.02 (s, 1 H), 3.61 (t, J = 7.2 Hz, 2 H), 2.41 (s, 3 H), 2.27 (t, J = 7.2 Hz, 2 H), 1.79 (quin, J = 7.2 Hz, 2 H); ^{13}C NMR (176 MHz, DMSO-d_6) δ ppm 173.8, 169.8, 166.2, 140.9, 138.6, 132.3, 132.0, 122.0, 118.7, 111.3, 39.5, 30.7, 23.8, 15.4; HRMS (ESI) m/z: 298.1189 found (calcd for $C_{16}H_{16}N_3O_3^+$, $[M + H]^+$ 298.1186).

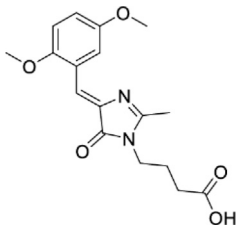

(*Z*)-4-(4-(2,5-dimethoxybenzylidene)-2-methyl-5-oxo-4,5-dihydro-1*H*-imidazol-1-yl)butanoic acid (DyeC acid, Figure S5C)

Yellow solid (2.51 g, 63%); mp = 148–151°C with decomposition; ^{1}H NMR (700 MHz, DMSO-d_6) δ ppm 12.10 (br. s., 1 H), 8.39 (s, 1 H), 7.26 (s, 1 H), 7.23–7.28 (m, 2 H), 3.83 (s, 3 H), 3.74 (s, 3 H), 3.59 (t, J = 7.2 Hz, 2 H), 2.38 (s, 3 H), 2.26 (t, J = 7.2 Hz, 2 H), 1.78 (quin, J = 7.2 Hz, 2 H); ^{13}C NMR (176 MHz, DMSO-d_6) δ ppm 173.8, 170.0, 163.8, 153.0, 152.9, 138.3, 122.9, 117.6, 117.1, 117.0, 112.2, 56.1, 55.4, 39.3, 30.7, 23.9, 15.4; HRMS (ESI) m/z: 333.1452 found (calcd for $C_{17}H_{21}N_2O_5^+$, $[M + H]^+$ 333.1445).

Preparation of 4-(4-((Z)-benzylidene)-2-((E)-styryl)-5-oxo-4,5-dihydro-1H-imidazol-1-yl)butanoic acids (Figure S5D)

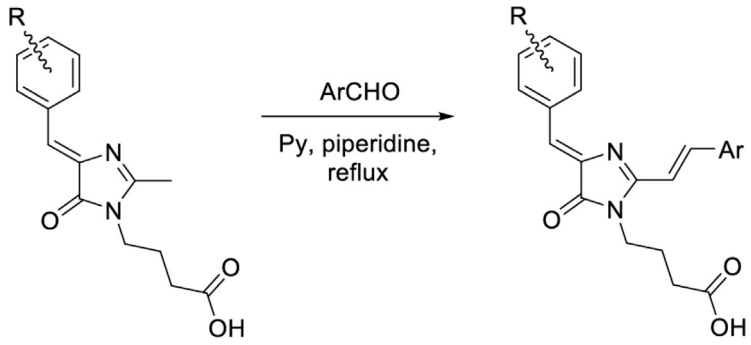

To the solution of (Z)-4-(4-benzylidene-2-methyl-5-oxo-4,5-dihydro-1H-imidazol-1-yl)butanoic acid (1 mmol) in pyridine (5 mL) piperidine (0.01 mL) and corresponding aldehyde (5 mmol) were added. The mixture was refluxed for 24 h and the solvent was evaporated. The residue

was dissolved with mixture EtOAc (200 mL) and AcOH (1 mL), washed brain (2 × 10 mL) and dried over Na_2SO_4. The solvent was evaporated and the product was purified by column chromatography (CH_2Cl_2-MeOH, 100/5).

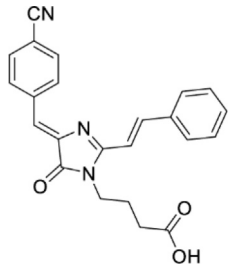

4-(4-((*Z*)-4-cyanobenzylidene)-2-((*E*)-styryl)-5-oxo-4,5-dihydro-1*H*-imidazol-1-yl)butanoic acid (DyeA acid, Figure S5E)

Yellow solid (275 mg, 71%); mp = 194–197°C; ^{1}H NMR (700 MHz, DMSO-d_6) δ ppm 12.29 (br. s., 1 H), 8.48 (d, J = 8.2 Hz, 2 H), 8.15 (d, J = 15.6 Hz, 1 H), 7.87–7.93 (m, 4 H), 7.45–7.52 (m, 3 H), 7.33 (d, J = 15.6 Hz, 1 H), 7.08 (s, 1 H), 3.81 (t, J = 7.3 Hz, 2 H), 2.32 (t, J = 7.0 Hz, 2 H), 1.80 (quin, J = 7.2 Hz, 2 H); ^{13}C NMR (176 MHz, DMSO-d_6) δ ppm 174.1, 169.8, 162.1, 142.0, 141.5, 139.0, 134.9, 132.3, 132.3, 130.5, 129.0, 128.6, 122.0, 118.8, 113.4, 111.2, 38.9, 30.6, 24.5; HRMS (ESI) m/z: 386.1510 found (calcd for $C_{23}H_{20}N_3O_3^+$, $[M + H]^+$ 386.1499).

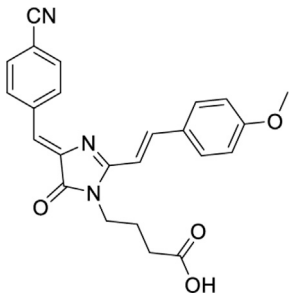

4-(4-((*Z*)-4-cyanobenzylidene)-2-((*E*)-4-methoxystyryl)-5-oxo-4,5-dihydro-1*H*-imidazol-1-yl)butanoic acid (DyeB acid, Figure S5F)

Orange solid (310 mg, 81%); mp = 217–220°C; ^{1}H NMR (700 MHz, DMSO-d_6) δ ppm 8.46 (d, J = 8.2 Hz, 2 H) 8.11 (d, J = 15.6 Hz, 1 H), 7.86–7.90 (m, 4 H), 7.20 (d, J = 15.6 Hz, 1 H), 7.04 (d, J = 8.8 Hz, 2 H), 7.01 (s, 1 H), 3.84 (s, 3 H), 3.79 (t, J = 7.3 Hz, 2 H), 2.27 (t, J = 7.0 Hz, 2 H), 1.78 (quin, J = 7.2 Hz, 2 H); ^{13}C NMR (176 MHz, DMSO-d_6) δ ppm 169.9, 162.5, 161.4, 142.0, 141.7, 139.2, 132.3, 132.1, 130.6, 127.6, 120.9, 118.9, 114.5, 114.5, 110.9, 110.6, 55.4, 39.0, 31.3, 24.8; HRMS (ESI) m/z: 416.1609 found (calcd for $C_{24}H_{22}N_3O_4^+$, $[M + H]^+$ 416.1605).

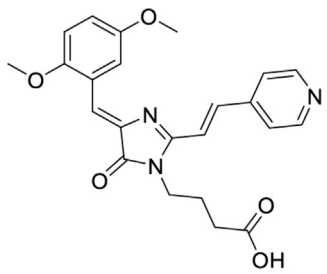

4-(4-((*Z*)-2,5-dimethoxybenzylidene)-2-((*E*)-2-(pyridin-4-yl)vinyl)-5-oxo-4,5-dihydro-1*H*-imidazol-1-yl)butanoic acid (DyeD acid, Figure S5G)

Orange solid (290 mg, 69%); mp = 254-257°C; ^{1}H NMR (700 MHz, DMSO-d_6) δ 12.21 (br. s., 1 H), 8.67 (d, J = 5.9 Hz, 2 H), 8.54 (s, 1 H), 7.93 (d, J = 15.8 Hz, 1 H), 7.79 (d, J = 5.9 Hz, 2 H), 7.54 (d, J = 15.6 Hz, 1 H), 7.42 (s, 1 H), 7.03–7.08 (m, 2 H), 3.86 (s, 3 H), 3.79–3.84 (m, 5 H), 2.31 (t, J = 7.1 Hz, 2

H), 1.80 (quin, J = 7.2 Hz, 2 H); ^{13}C NMR (201 MHz, DMSO-d_6) δ ppm 174.0, 169.8, 159.2, 153.4, 153.0, 150.3, 141.9, 138.7, 137.5, 123.1, 122.0, 119.2, 118.4, 118.3, 116.3, 112.4, 56.1, 55.3, 38.8, 30.4, 24.5; HRMS (ESI) m/z: 422.1719 found (calcd for $C_{23}H_{24}N_3O_5^+$, $[M + H]^+$ 422.1710).

Preparation of 4-(4-((Z)-benzylidene)-5-oxo-4,5-dihydro-1H-imidazol-1-yl)-N-(2-(2,5-dioxo-2,5-dihydro-1H-pyrrol-1-yl)butanamide (Figure S5H)

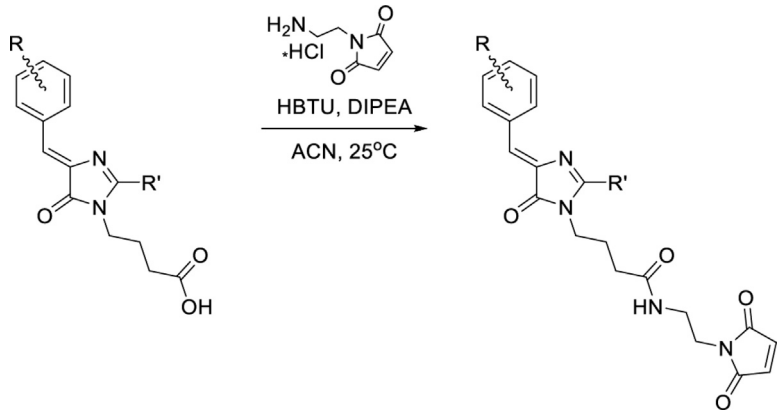

To the solution of 4-(4-((Z)-benzylidene)-2-((E)-styryl)-5-oxo-4,5-dihydro-1H-imidazol-1-yl)butanoic acids (0.1 mmol) in acetonitrile (2 mL) 1-(2-aminoethyl)-1H-pyrrole-2,5-dione hydrochloride (20 mg, 0.114 mmol), HBTU (40 mg, 0.106 mmol) and DIPEA (0.075 mL, 0.4 mmol) were added. The mixture was stirred for 12 h at room temperature. The mixture was dissolved with $CHCl_3$ (200 mL), washed with a saturated solution of $NaHCO_3$ (6 × 50), HCl (1%, 30 mL) and brain (2 × 50 mL) and dried over Na_2SO_4. The solvent was evaporated and the product was purified by column chromatography (CH_2Cl_2-MeOH, 100/5).

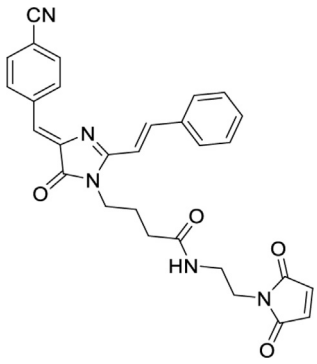

4-(4-((*Z*)-4-cyanobenzylidene)-2-((*E*)-styryl)-5-oxo-4,5-dihydro-1*H*-imidazol-1-yl)-*N*-(2-(2,5-dioxo-2,5-dihydro-1*H*-pyrrol-1-yl) butanamide (DyeA maleimide, Figure S5I)

Yellow solid (38 mg, 75%); mp = 153–157°C; ^{1}H NMR (700 MHz, DMSO-d_6) δ ppm 8.48 (d, J = 8.4 Hz, 2 H), 8.14 (d, J = 15.6 Hz, 1 H), 7.98 (t, J = 5.9 Hz, 1 H), 7.90–7.94 (m, 4 H), 7.46–7.53 (m, 3 H), 7.36 (d, J = 15.8 Hz, 1 H), 7.08 (s, 1 H), 6.94 (s, 2 H), 3.76 (t, J = 7.2 Hz, 2 H), 3.45 (t, J = 5.8 Hz, 2 H), 3.19 (q, J = 5.9 Hz, 2 H), 2.08 (t, J = 7.2 Hz, 2 H), 1.77 (quin, J = 7.2 Hz, 2 H); ^{13}C NMR (176 MHz, DMSO-d_6) δ ppm 171.6, 171.0, 169.8, 162.2, 142.0, 141.6, 139.0, 134.9, 134.4, 132.3, 132.3, 130.5, 129.0, 128.7, 122.0, 118.8, 113.5, 111.2, 38.2, 37.1, 36.9, 31.7, 24.8; HRMS (ESI) m/z: 508.1989 found (calcd for $C_{29}H_{26}N_5O_4^+$, $[M + H]^+$ 508.1979).

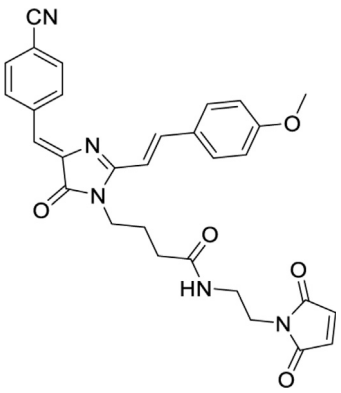

4-(4-((*Z*)-4-cyanobenzylidene)-2-((*E*)-4-methoxystyryl)-5-oxo-4,5-dihydro-1*H*-imidazol-1-yl)-N-(2-(2,5-dioxo-2,5-dihydro-1H-pyrrol-1-yl)ethyl)butanamide (DyeB maleimide, Figure S5J)

Orange solid (33 mg, 61%); mp = 181-184°C; ^{1}H NMR and ^{13}C NMR – see Figure S6; HRMS (ESI) m/z: 538.2089 found (calculated for $C_{30}H_{28}N_5O_5^+$, $[M + H]^+$ 538.2085).

The structure of this compound was analyzed by two-dimensional NMR spectroscopy. The compound is represented in solution by two isomers in approximately 1:1 ratio. However, these isomers easily passed into each other in solution and the ratio could change with time. To elucidate the structure of both isomers, we performed full chemical shift assignment based on the HSQC, COSY, ^{13}C- and ^{15}N-HMBC spectra and measured the heteronuclear vicinal H-C J-couplings, using the PIP-HSQCMBC experiment.[96]

According to the NMR data, this compound is present in solution as a mixture of Z and E isomers across the C1′-C2′ double bond. The major state corresponds to the Z-isomer, which is supported by the large magnitude of H1′-H2′ ^{3}J-coupling (15.6 Hz), corresponding to the trans orientation of protons. In the minor state, the same J-coupling equals 13.0 Hz, which corresponds to the cis orientation. The maximal chemical shift difference between the two states is observed for the double bond protons H1′ and H2′, and exceeds 0.8 ppm for both of them.

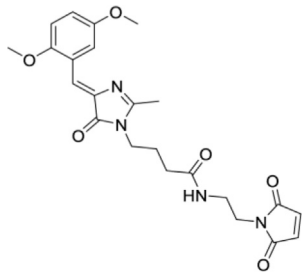

(*Z*)-4-(4-(2,5-dimethoxybenzylidene)-2-methyl-5-oxo-4,5-dihydro-1*H*-imidazol-1-yl)-*N*-(2-(2,5-dioxo-2,5-dihydro-1*H*-pyrrol-1-yl)ethyl)butanamide (DyeC maleimide, Figure S5K)

Yellow solid (24 mg, 53%); mp = 125–128°C with decomposition; ^{1}H NMR and ^{13}C NMR see Figure S7; HRMS (ESI) m/z: 455.1915 found (calculated for $C_{23}H_{27}N_4O_6^+$, $[M + H]^+$ 455.1925).

The structure of this compound was analyzed by two-dimensional NMR spectroscopy. The compound is represented in solution by two isomers in approximately 1:2 ration (E and Z). However, these isomers easily passed into each other in solution and the ratio could change with time. To elucidate the structure of both isomers, we performed full chemical shift assignment based on the HSQC, COSY, ^{13}C- and ^{15}N-HMBC spectra and measured the heteronuclear vicinal H-C J-couplings, using the PIP-HSQCMBC experiment.[96]

DyeC maleimide exists as two Z-E isomers across the C6-C4 double bond. The major form is the Z-isomer, which follows directly from the value of C6H-C5 J-coupling (4.8 Hz), which is indicative of the cis arrangement of the C6 proton and C5 carbon. In contrast, the corresponding J-coupling in the minor configuration of DyeC maleimide equaled 9.9 Hz, implying the trans arrangement of the proton and carbon and E-configuration of the double bond. This is supported by the chemical shift differences between the states, which are at most pronounced for the C6 carbon and exceed 10 ppm.

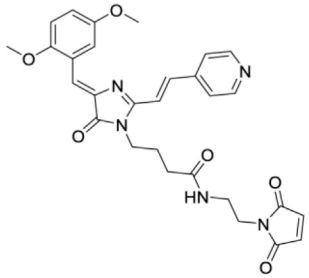

4-(4-((*Z*)-2,5-dimethoxybenzylidene)-2-((*E*)-2-(pyridin-4-yl)vinyl)-5-oxo-4,5-dihydro-1*H*-imidazol-1-yl)-*N*-(2-(2,5-dioxo-2,5-dihydro-1*H*-pyrrol-1-yl)ethyl)butanamide (DyeD maleimide, Figure S5L)

Orange solid (22 mg, 41%); mp = 204-207°C; ^{1}H NMR (700 MHz, DMSO-d_6) δ ppm 8.69 (d, J = 6.1 Hz, 2 H), 8.53 (t, J = 1.7 Hz, 1 H), 7.99 (t, J = 6.2 Hz, 1 H), 7.92 (d, J = 15.8 Hz, 1 H), 7.82 (d, J = 5.9 Hz, 2 H), 7.59 (d, J = 15.6 Hz, 1 H), 7.42 (s, 1 H), 7.05 (d, J = 1.7 Hz, 2 H), 6.95 (s, 2 H), 3.86 (s, 3 H), 3.83 (s, 3 H), 3.75 (t, J = 7.4 Hz, 2 H), 3.46 (t, J = 5.8 Hz, 2 H), 3.20 (q, J = 5.8 Hz, 2 H), 2.07 (t, J = 7.3 Hz, 2 H), 1.76 (quin, J = 7.3 Hz, 2 H); ^{13}C NMR (201 MHz, DMSO-d_6) δ ppm 171.7, 171.0, 169.7, 159.3, 153.4, 153.0, 150.3, 142.0, 138.7, 137.5, 134.4, 123.0, 122.1, 119.2, 118.5, 118.4, 116.2, 112.5, 56.2, 55.3, 39.0, 37.1, 36.9, 31.7, 24.9; HRMS (ESI) m/z: 544.2198 found (calcd for $C_{29}H_{30}N_5O_6^+$, $[M + H]^+$ 544.2191).

Rec and Rec_{C39D} expression, purification and labeling

DNA constructs

The genetic construct for bacterial expression of Rec from Bos taurus (UniProt ID P21457) was prepared by inserting corresponding cDNA into a pET11d vector (Novagen, USA) between NcoI and BamHI restriction sites under the control of the T7 phage promoter as previously described.[97] The construct for the expression of the cysteine-free Rec mutant C39D (Rec_{C39D}) was obtained by site-directed mutagenesis using the bovine Rec gene in a pET-11d plasmid as a template as previously described.[98]

Rec and Rec_{C39D} expression

Rec and Rec_{C39D} were produced in *Escherichia coli* strain BL21-CodonPlus(DE3)-RIL-X (Agilent, USA) co-transformed with a pBB131 plasmid, carrying a gene for the N-myristoyl transferase-1 from Saccharomyces cerevisiae (UniProt ID P14743). To obtain the myristoylated form of Rec, cells were cultivated for 5 h (250 rpm, 37°C) in the presence of myristic acid (20 mg/L) added to the medium immediately prior to the induction of the expression with 0.5 mM isopropyl β-D-1-thiogalactopyranoside. Rec/Rec_{C39D}-containing fractions were obtained by exposing cells to repetitive freeze-thaw cycles in lysis buffer (50 mM Tris-HCl, pH = 7.5, 5 mM $MgCl_2$, 1 mM EDTA, 0.1 mM PMSF, 3 mM DTT) and treatment of the resulting suspension with lysozyme (25–50 μg/mL, 20 min, on ice) with subsequent centrifugation (12,000 ×g, 20 min, 4°C).

Rec and Rec_{C39D} purification

For the primary isolation of Rec and Rec_{C39D}, the obtained fractions were mixed on ice with calcium chloride (3 mM), loaded onto a Phenyl Sepharose column (Cytiva, USA), equilibrated with a buffer (20 mM Tris-HCl, pH = 7.5, 2 mM $CaCl_2$, 2 mM $MgCl_2$ and 1 mM DTT), and the target proteins were eluted with the same buffer containing 1 mM EGTA instead of $CaCl_2$. For the final purification and concentration of recoverin forms, the EGTA fractions were loaded onto a HiTrap Q FF column (Cytiva, USA) equilibrated with a buffer (20 mM Tris-HCl, pH = 7.5, 1 mM DTT), and the proteins were eluted using a linear salt gradient from 0 to 1 M NaCl. After the purification, Rec and Rec_{C39D} were dialyzed against a storage buffer (20 mM Tris-HCl, pH = 7.5, 1 mM DTT), aliquoted, and stored at −80°C (Figure S8A). The degree of Rec myristoylation in the obtained preparations was determined by analytical HPLC using Luna C18 reversed-phase column (Phenomenex) in the acetonitrile-water system and was more than 95% (Figures S8B and S8C). The final yield was 25–30 mg of the Rec/Rec_{C39D} per liter of bacterial culture.

Rec labeling

Rec samples were transferred to a labeling buffer (50 mM HEPES, pH = 7.0, 5 mM EGTA) using 10 kDa MWCO Amicon Ultra centrifugal filter unit (Merck Millipore, USA), and concentrated to 0.5 μg/mL. 20-fold molar excess of each of the dyes (DyeA, DyeB, DyeC or DyeD) dissolved in DMSO was then added to Rec preparation, yielding the final DMSO concentration of 6% (v/v). The mixture was incubated for 16 h at 4°C with constant rotation on an orbital shaker (15 rpm) in the dark. The unbound fluorescent labels were washed out with a Rec-washing buffer (50 mM HEPES pH = 8.0) in a Stirred Cell Model 8003 (Millipore), with a 10 kDa MWCO regenerated cellulose filter (Millipore). The protein concentration and labeling efficiency were calculated from the absorption spectra as described below (see "Labeled proteins absorption and emission measurements").

A_{2A}AR expression, purification, and labeling

DNA construct

The nucleotide sequence of the human *ADORA2A* gene encoding A_{2A}AR (2–316 aa) (UniProt ID C9JQD8) was obtained from the cDNA Resource Center (cdna.org, #ADRA2A0000) and modified for expression in *Spodoptera frugiperda*. The final gene construct was complemented from the 5′-terminus by nucleotide sequences of the hemagglutinin signal peptide (MKTIIALSYIFCLVFA), FLAG tag (DYKDDDDK), linker (AMGQPVGAP), and from the 3′-terminus by the 10×His-tag nucleotide sequence and inserted into a pFastBac1 vector (Invitrogen) via the BamHI(5′) and HindIII(3′) restriction sites. The $L225^{6.27}C$ mutation was introduced by PCR. A snake-plot representation of the protein construct is shown in Figure S9A.

A_{2A}AR expression

A high-titer recombinant baculovirus (>10^9 viral particles per mL) for A_{2A}AR expression in insect cells (Sf9) was obtained following a modified Bac-to-Bac system protocol (Invitrogen). Recombinant baculoviruses were generated by transfecting 2.5 μg of a transfer bacmid into Sf9 cells (2.5 mL at a density of 10^6 cells/mL) using 3 μL of X-tremeGENE HP DNA Transfection Reagent (Roche) and 100 μL Transfection Medium (Expression Systems). The cell suspension was incubated for 4 days with shaking using a Shel Lab incubator at 27°C and 300 rpm in 24-deep well U-bottom plates covered with Breathe-Easy membranes (Greiner BioOne). A P0 viral stock was isolated by centrifugation at 2000 ×g for 5 min, and used to produce a high-titer baculovirus stock (P1): 40 mL of cells at 2 ×10^6 cells/mL density were infected with 2.5 mL supernatant, and grew for 72 h with shaking at 27°C and 120 rpm (Innova 44, New Brunswick). Sf9 cells at a cell density of 2–3 ×10^6 cells/mL were infected with the P1 virus at the multiplicity of infection equal to 5. Expression was performed with shaking at 27°C and 120 rpm (Innova 44, New Brunswick), in 1 L vent-cap flasks (Corning). Cells were harvested by centrifugation at 2,000 ×g for 10 min, after 48 h post infection, and stored at −80°C until further use. Cell counts, viral titers and expression levels were measured by flow cytometry on a BD Accuri C6 (BD Biosciences).

A_{2A}AR purification and labeling

The biomass obtained from 1 L of cell culture was thawed on ice with 200 μL of a protease inhibitor cocktail (500 μM AEBSF (Gold Biotechnology), 1 μM E−64 (Cayman Chemical), 1 μM leupeptin (Cayman Chemical), 150 nM aprotinin (AG Scientific)) in a low-salt buffer (10 mM HEPES pH = 7.5, 10 mM $MgCl_2$, 20 mM KCl) to 100 mL (scaled if necessary). The mixture was homogenized in a high-tight 100 mL Potter douncer on ice, centrifuged for 20 min at 4°C and 220,000 ×g. The supernatant was discarded, and the pellet was resuspended in 100 mL of a high-salt buffer (10 mM HEPES pH = 7.5, 10 mM $MgCl_2$, 20 mM KCl, 1 M NaCl) supplemented with 100 μL protease inhibitor cocktail, centrifuged for 30 min at 4°C and 220,000 ×g. The resuspension and centrifugation were repeated one more time.

Fluorescent labeling and all further procedures were carried out at 4°C in the dark or under a dim red light and with constant rotation on an orbital shaker (15 rpm) during any incubation.

The washed membranes obtained from 1 L of cell culture were resuspended in 20 mL of a labeling buffer (20 mM HEPES pH 7.0, 10 mM $MgCl_2$, 20 mM KCl, 4 mM theophylline, 50 μL protease inhibitor cocktail), mixed with a dye solution (2 mg of sulfo-Cy5 maleimide (Lumiprobe), 2 mg Cy3 maleimide (Lumiprobe), 2 mg TMR-5 maleimide (Lumiprobe), 4 mg of DyeB, 2 mg of bimane, or 4 mg DyeC, dissolved in 60 μL of DMSO), and incubated for 16 h. After labeling, membrane fractions were pelleted by ultracentrifugation at 220,000 ×g for 30 min and washed three times with the high-salt buffer to remove unbound fluorescent labels.

The labeled membranes were homogenized in 50 mL of solubilization buffer (50 mM HEPES pH = 7.5, 800 mM NaCl, 5% v/v glycerol, 0.5/0.1% w/v DDM/CHS (Sigma), 4 mM theophylline (Sigma), 50 μL protease inhibitor cocktail). Receptor solubilization was carried out for 4 h. The insoluble debris was eliminated then by centrifugation for 1 h, 650,000 ×g, while the target protein remained in the supernatant. The supernatant was incubated with 500 μL of a TALON resin (Clontech) for 16 h.

The resin was washed with 10 column volumes (CV) of wash buffer 1 (50 mM HEPES pH = 7.5, 800 mM NaCl, 10% v/v glycerol, 25 mM imidazole, 0.1/0.02% w/v DDM/CHS, 10 mM $MgCl_2$, 8 g/mol ATP (Sigma), 4 mM theophylline), then 5 CV of wash buffer 2 (50 mM HEPES pH = 7.5, 800 mM NaCl, 10% v/v glycerol, 50 mM imidazole, 0.05/0.01% w/v DDM/CHC, and 4 mM theophylline). The receptor was eluted with 3 CV of elution buffer (25 mM HEPES pH = 7.5, 800 mM NaCl, 10% v/v glycerol, 220 mM imidazole, 0.01/0.002% w/v DDM/CHS, and 4 mM theophylline). The eluted receptor was desalted from imidazole using a size-exclusion PD10 column (GE Healthcare) equilibrated with the desalt buffer (25 mM HEPES pH = 7.5, 800 mM NaCl, 0.01/0.002% w/v DDM/CHS).

The labeled and purified receptor was concentrated using a 30 kDa MWCO filter (Merck, Amicon Ultra) to 10–15 μM. Receptor purity and homogeneity were assessed by SDS-PAGE and analytical size-exclusion chromatography (SEC) accordingly (Figures S9B–S9D).

A_{2A}AR reconstitution into ND

The Membrane Scaffold Protein 1D1 (MSP1D1) for ND was expressed in the *Escherichia coli* strain BL21(DE3) using a gene (nucleotide sequence was taken from McLean M.A. at al.[99] and synthesized *de novo*, Genescript) with an N-terminal 6×His-tag and a TEV-protease site cloned into a pET28a vector between the NcoI and HindIII restriction sites (Table S3). MSP1D1 was purified using IMAC Ni-NTA Agarose (Qiagen) with further cleavage of 6×His-tag by TEV protease. The lipid mixture of POPC:POPG (Avanti Polar Lipids) in chloroform was prepared at a molar ratio 7:3. The lipid film was dried under a gentle nitrogen gas stream, followed by removal of the solvent traces under vacuum

first with the use of a rotary evaporator (Hei-VAP Ultimate ML/G1, Heidolph) and then with deep vacuum oil-free pump (ChemStar Dry Oil-Free Deep Vacuum System) overnight, next day solubilized in 100 mM sodium cholate (Sigma) and stored at −80°C until further use.

The purified A_{2A}AR (WT or L225C$^{6.27}$) in DDM/CHS micelles was mixed with MSP1D1 and the POPG:POPC lipid mixture at a molar ratio A_{2A}AR:MSP1D1:lipids = 1:5:50. The final sodium cholate concentration was maintained in the range of 25–30 mM, the typical final receptor concentration was 0.5-0.6 mg/mL. After 1 h pre-incubation, the mixture was incubated overnight with wet Bio-Beads SM-2 (0.14 g of beads for 1 g of detergent were washed in methanol and equilibrated with 25 mM HEPES, pH = 7.5, 150 mM NaCl). The next morning, a fresh portion of Bio-Beads for an additional 4 h incubation was added, beads were discarded and the supernatant containing reconstituted into ND A_{2A}AR was incubated for 4 h with 250 μL of Ni-NTA resin (Qiagen) for separating from empty ND. The protein was eluted in the elution buffer (25 mM HEPES pH = 7.5, 150 mM NaCl, 150 mM imidazole), and then desalted from imidazole using size-exclusion PD-10 column equilibrated with desalt ND buffer (25 mM HEPES pH = 7.5, 150 mM NaCl).

A_{2A}AR reconstituted into ND was concentrated using a 100 kDa MWCO filter (Merck, Amicon Ultra) to 10–15 μM. Labeling efficiency was calculated from the absorption spectrum measured as described below (see "Concentration and labeling efficiency calculations").

SDS-PAGE, SEC and nanoDSF

The samples were subjected to SDS-PAGE using a Mini-Protean IV system (Bio-Rad) with polyacrylamide gel (5% concentrating gel with AA:bisAA ratio of 29:1 and 15% resolving gel with 19:1 AA:bisAA ratio). The protein was loaded in the amount of 5 μg of receptor per lane previously mixed with a loading buffer (25 mM Tris pH = 6.8, 25% v/v glycerol, 0.25% SDS, bromophenol blue) without preheating and stained after separation with Coomassie Brilliant Blue R-250.

Analytical size-exclusion chromatography was performed on a Dionex Ultimate 3000 instrument (Thermofisher) equipped with a Nanofilm Sec 250 (Sepax technologies, cat# 201250-4625) gel filtration analytical column. The column was equilibrated with chromatographic buffer: 0.05/0.01% w/v DDM/CHC, 25 mM HEPES pH = 7.5, 500 mM NaCl, 20 mM $MgCl_2$, 2% v/v glycerol. For ND, no detergents were added in the chromatographic buffer. The flow rate was 0.35 mL/min, protein absorption was detected at 280 nm, and 40 μL of the sample was injected.

For the low-volume differential scanning fluorimetry (nanoDSF), protein samples containing 2 μM of A_{2A}AR (labeled with sulfo-Cy5 maleimide, Cy3 maleimide, TMR-5 maleimide, or DyeC) and 100 μM of the ligand (ZM241385, NECA) or without a ligand for the apo state were prepared with the total volume of 15 μL. After 20 min the incubation at 4°C, the 10 μL of the mixtures were loaded in standard grade Prometheus NT.48 capillaries (Nanotemper) and subjected to a linear increase in the temperature from 25°C to 90°C at a 1°C/min rate using a Prometheus NT.48 Nano-DSF instrument (NanoTemper Technologies). The temperature-dependent changes in the intrinsic fluorescence were measured at the emission wavelengths of 350 nm with excitation wavelengths of 280 nm. The data for the first derivative were offset and normalized so that the maximum of the derivative corresponded to 1 and the minimum to 0. The T_m values were determined as the maxima of the first derivatives of the fluorescence intensities using the PR.ThermControl software (NanoTemper Technologies).

Free dye absorption and emission measurements

Free dye absorption and emission measurements UV-VIS spectra of free dyes were recorded on a Varian Cary 100 (Agilent Varian) spectrophotometer. Fluorescence excitation and emission spectra were recorded on a Cary Eclipse (Agilent Technologies) fluorescence spectrophotometer. The fluorescence quantum yields were calculated according to the procedure described in the literature[100] with the use of Coumarine 153 as a standard. The quantum yield was calculated by the formula:

$$\Phi_x = \Phi_{st} \times \frac{F_x}{F_{st}} \times \frac{f_{st}}{f_x} \times \frac{{n_x}^2}{{n_{st}}^2} \quad \text{(Equation 1)}$$

where F is the area under the emission peak, f is the absorption factor (see below), n is the refractive index of the solvent, Φ is the fluorescence quantum yield, the subscript x corresponds to the dye of interest, the subscript st – for standards.

$$f = 1 - 10^{-A} \quad \text{(Equation 2)}$$

where A is the absorbance at the excitation wavelength.

The molar extinction coefficient was calculated by the formula:

$$\varepsilon = \frac{A}{cl} \quad \text{(Equation 3)}$$

where A is the absorbance maximum, c is the molar concentration, l is the pathlength.

Absorption and emission measurements of labeled proteins

All absorption and emission measurements for both labeled A_{2A}AR and Rec were carried out at 25°C on a Synergy H4 (Agilent BioTek) plate reader with Take3 Microvolume Plates; 2.5 μL of sample was added in each microspot. After measurements, the spectrum of the buffer was measured in each microspot and subtracted from the sample spectra. All obtained data were analyzed using the GraphPad Prizm 9.4.1 software.

Concentration and labeling efficiency calculations

Protein concentrations were calculated from absorption at 280 nm using the molar extinction coefficients of 24,075 $M^{-1}cm^{-1}$ (Rec), 51,880 $M^{-1}cm^{-1}$ ($A_{2A}AR$), 18,200 $M^{-1}cm^{-1}$ (MSP1D1) and the light pathlength of 0.05 cm.

Labeling efficiencies for proteins with DyeA, DyeB, DyeC, DyeD, sulfo-Cy5, Cy3, TMR-5, and bimane were estimated by measuring their absorbance at 420, 440, 400, 390, 646, 552, 550 and 390 nm using the extinction coefficients of 19,000 $M^{-1}cm^{-1}$ [3], 21,000 $M^{-1}cm^{-1}$ [3], 14,000 $M^{-1}cm^{-1}$ [3], 15,000 $M^{-1}cm^{-1}$ [3], 250,000 $M^{-1}cm^{-1}$, 150,000 $M^{-1}cm^{-1}$, 84,000 $M^{-1}cm^{-1}$, and 5,000 $M^{-1}cm^{-1}$ respectively.

Labeled Rec emission measurements

1 mM $CaCl_2$ and 1 mM EGTA were added separately to the labeled protein in Rec-washing buffer (50 mM HEPES pH = 8.0) with final concentrations of 100 μM for $CaCl_2$ or EGTA in a total volume of 9 μL: Rec concentration was equal between two protein samples labeled with same dye and varied in a range of 2–10 μM for samples labeled with different dyes. After 20 min of incubation at 4°C in the dark, fluorescence emission spectra of Rec with DyeA, DyeB, and DyeC were then measured with excitation at 440 nm, 460 nm, and 410 nm, respectively, and a 9 nm emission bandwidth.

Labeled $A_{2A}AR$ emission measurements

Ligands (ZM241385 (Cayman Chemical), SCH58261 (Tocris), Adenosine (Tocris), HMA (Merck) or NECA (Tocris)) were dissolved in DMSO to make 100 mM stock solutions. Then 1 mM and 100 μM stock solutions of ligands in the desalt ND buffer were prepared. The samples with labeled $A_{2A}AR$ (WT or $L225^{6.27}C$) and 100 μM of a ligand (or no ligand for apo sample) were prepared in the desalt ND buffer in a final volume of 9 μL. The final protein concentrations were consistent across different ligands within the same run of the measurements, but varied between 2 and 10 μM for different receptor batches.

After 20 min incubation at 4°C in the dark, emission spectra of $A_{2A}AR$ with sulfo-Cy5, Cy3, TMR-5, DyeB, DyeC, and bimane were measured with excitation at 630 nm, 530 nm, 520 nm, 460 nm, 410 nm, and 390 nm respectively, and a 9 nm emission bandwidth.

Emission spectra for protein samples labeled with sulfo-Cy5, Cy3, TMR-5, and bimane were recorded with six technical repeats in one protein purification. Emission spectra for protein samples with DyeB and DyeC from at least three different protein purifications were recorded with at least three technical repeats for each purification. To compensate for differences of protein concentration and labeling efficiencies between different purification batches, all measured fluorescence spectra were normalized to the maximum of the fluorescence spectra of $A_{2A}AR_{L225C}$-DyeC with NECA measured in the same run and averaged over at least three technical replicas.

Displacement experiments

Two experiments were conducted to demonstrate the reversibility of conformational changes upon ligand displacement. In the beginning of each experiment, three samples of apo $A_{2A}AR_{L225C}$-DyeC in the desalt ND buffer were prepared, 1 μg of receptor in each. The initial volumes of 8.1 μL, 7.8 μL and 6.9 μL were selected to amount to equal final volumes of 9 μL after all further additives. The first experiment was carried out to replace NECA with ZM241385. 0.9 μL of 100 μM NECA were added to each of the three $A_{2A}AR_{L225C}$-DyeC samples. After 20 min incubation at 4°C, an emission spectrum using excitation at 410 nm was measured for the first sample containing 10 μM of NECA. Then 0.27 μL of 1 mM ZM241385 were added to the remaining two samples. After 20 min incubation at 4°C, the emission spectrum of the second sample containing 10 μM of NECA and 30 μM of ZM241385 was measured. Finally, 0.9 μL of 1 mM NECA was added to the remaining third sample to final cumulative concentration of 30 μM of ZM241385 and 110 μM of NECA. The emission spectrum of the third sample was measured after 20 min incubation at 4°C. In the second experiment, the same steps were repeated, but the order of adding ZM241385 and NECA was opposite. The final protein concentration was 2 μM in each measured sample.

Molecular dynamics simulations

Protein models were prepared using the structure of a thermostabilized $A_{2A}AR$ in complex with ZM241385 (PDB ID: 3PWH,[62]) and the structure of $A_{2A}AR$ in complex with mini-Gs (PDB ID: 5G53,[101]) for inactive and active states, respectively. The thermostabilized mutations were mutated back to the native amino acids and the missing regions were added using MODELLER.[91] All ionizable amino acids were modeled in their standard ionization state at pH = 7.

The DyeC label was attached to the position $L225^{6.27}C$ by aligning its backbone moiety with the corresponding group of the original amino acid mutated to cysteine. Both active and inactive protein models were embedded in a lipid bilayer consisting of POPC and solvated using the CHARMM-GUI server.[92] The final models contained 203 POPC lipids, 21,674 water molecules, 86/95 Na^+/Cl^- ions in the active state (97,334 atoms in total, box dimensions 9.09 × 9.09 × 11.48 nm), and 205 POPC lipids, 25,406 water molecules, 98/107 Na^+/Cl^- ions in the inactive state (108,682 atoms in total, box dimensions 8.73 × 8.73 × 14.04 nm).

For each state, we produced two simulation replicates starting from two alternative orientations of DyeC (Figure S10) to overcome the problem of slow DyeC flipping from one side of the TM5-ICL3-TM6 fragment to the other side. In order to generate the two alternative starting conformations with the fluorescent label oriented on the opposite sides of the TM5-ICL3-TM6 fragment (i.e., pointing toward and outwards the protein center), we run short steered MD simulations with the moving harmonic potential (force constant of 1000 kJ/mol/nm^2) applied to one of the carbon atoms of the dimethoxybenzene ring pulling it away from the protein center-of-mass with the constant velocity of 10^{-4} nm/ps. These steered simulations were conducted until the label flipped across ICL3 (~30 ns) and resulted in four starting

conformations, i.e., two alternative label conformations for each state, active and inactive. The starting models were subjected to the standard CHARMM-GUI equilibration comprising a steep descent minimization followed by several short equilibration simulations, ~2 ns in total, with the harmonic restraints applied to the protein and lipids.

After equilibrating the starting models according to the protocol described above, we performed metadynamics MD simulations to estimate the three-dimensional free energy surfaces for the fluorescent label in the active/inactive states. Metadynamics is an enhanced sampling technique, which allows to reconstruct free energy profiles/surfaces along selected collective variable(s) by adding numerous repulsive potentials or "hills" (typically, Gaussian-shaped) to the total potential of the system forcing the latter to explore its configurational space faster and broader.[76,77] We have chosen three projections of the vector connecting the Cα atom of the labeled cysteine residue with the proximal carbon atom of its dimethoxybenzene ring onto the three Cartesian axes as the collective variables biased in the metadynamics simulations since they provide a straightforward and efficient way to describe the general orientation of the fluorescent label. Gaussian hills with the width of 0.1 nm and the height of 0.25 kJ/mol were added every 0.5 ps. The grid was used to efficiently store the accumulated hills. Each metadynamics simulation was run for 500 ns. The convergence of the simulations was estimated by calculating the volume explored by the label using the custom script available at https://github.com/porekhov/A2a_GFP_core_dyes. The cumulative explored volume plotted as a function of simulation time is shown in Figure S10.

Throughout the equilibration and metadynamics simulations, positional restraints were applied to Cα atoms of the transmembrane region of A_{2A}AR as well as to the intracellular segment of TM6 encompassing the labeling position 225 and its neighboring amino acids to preserve the protein state and to prevent fluctuations of the label's Cα atom, which was used as the reference point for calculation of the collective variables. Apart from it, we also applied dihedral restraints (force constant of 1000 kJ/mol/rad^2) to the backbone atoms of the solvent-exposed protein regions in the α-helical conformation.

Since the relocation of the fluorescent label from one side of the TM5-ICL3-TM6 fragment to the opposite side is a relative slow process particularly hindered by the restraints applied to the protein backbone and limiting the thorough sampling of label orientations, we run duplicate metadynamics simulations for each state starting from two alternative conformations of the label obtained as noted above.

Additionally, four unbiased simulations (i.e., without any external forces applied to a system) were run to estimate mobility of the DyeC label in the active and inactive A_{2A}AR states starting from two alternative label orientations similar to the metadynamics simulations (see above). Each simulation was carried out for 1000 ns. The autocorrelation function was calculated as a measure for the mobility of fluorescent label using the rotacf tool in GROMACS according to the following expression, $ACF(t) = \langle \mathbf{v}(\tau) \cdot \mathbf{v}(\tau+t) \rangle_\tau$, where $\mathbf{v}$ is a vector describing the orientation of the fluorescent label and defined by Cα and the proximal carbon atom of the dimethoxybenzene ring of DyeC.

All MD simulations were performed by GROMACS version 2022.3[93] with the PLUMED plugin, version 2.8.1[102] allowing for metadynamics. A time step of 1–2 fs was used for equilibration simulations (3 × 125 ps with the 1-fs time step followed by 3 × 500 ps with the 2-fs time step), while all production metadynamics and unbiased simulations were performed with a 5 fs time step allowed by repartitioning the mass of heavy atoms into the bonded hydrogen atoms[103] and the LINCS constraint algorithm.[104] Production simulations were run in NVT ensemble with v-rescale thermostat (τ_T = 1.0 ps, T_{ref} = 303.15 K), van der Waals interactions were treated using the cut-off scheme, electrostatics – using PME.

The Amber99SB-ILDN force field was used for the protein, lipids, and ions[105] along with the TIP3P water model. The topology for the fluorescent label was obtained using Antechamber[106] with some dihedral parameters adopted from.[107] Conformation of the label was preliminary optimized at the DFT level with B3LYP functional and Def2-SVP/Def2/J basis set in Orca.[94]

QUANTIFICATION AND STATISTICAL ANALYSIS

Analysis of the integrated intensities and I_{520}/I_{460}

The data in Figures 3C and 3D represent the mean ± SD. The protein concentration was maintained at 10 μM, all ligands were added at a saturating concentration of 100 μM. The significance level is given according to the ordinary one-way ANOVA with the post hoc Tukey HSD test: $^{**}p < 0.005$, $^{*}p < 0.05$, ns – not significant. The number of repeats for each ligand is provided in Table S2. The statistical analysis was performed using Prism 9.4.1 software (GraphPad).